Structural and mechanistic insight into ribosomal ITS2 RNA processing by nuclease-kinase machinery

Jiyun Chen,[1,†] Hong Chen,[1,†] Shanshan Li,[2,†] Xiaofeng Lin,[1] Rong Hu,[1] Kaiming Zhang,[2,*] and Liang Liu[1,*]

[1] State Key Laboratory of Cellular Stress Biology, School of Life Sciences, Faculty of Medicine and Life Sciences, Xiamen University, Xiamen 361102, China and [2] MOE Key Laboratory for Cellular Dynamics and Division of Life Sciences and Medicine, University of Science and Technology of China, Hefei 230027, China

*For correspondence: kmzhang@ustc.edu.cn (K.Z.); liangliu2019@xmu.edu.cn (L.L.)

[†]These authors contributed equally to this work.

Abstract

Precursor ribosomal RNA (pre-rRNA) processing is a key step in ribosome biosynthesis and involves numerous RNases. A HEPN nuclease Las1 and a polynucleotide kinase Grc3 assemble into a tetramerase responsible for rRNA maturation. Here, we report the structures of full-length *Saccharomyces cerevisiae* and *Cyberlindnera jadinii* Las1-Grc3 complexes, and *Cyberlindnera jadinii* Las1. The Las1-Grc3 structures show that the central coiled coil domain of Las1 facilitates pre-rRNA binding and cleavage, while the Grc3 C-terminal loop motif directly binds to the HEPN active center of Las1 and regulates pre-rRNA cleavage. Structural comparison between Las1 and Las1-Grc3 complex exhibits that Grc3 binding induces conformational rearrangements of catalytic residues associated with HEPN nuclease activation. Biochemical assays identify that Las1 processes pre-rRNA at the two specific sites (C2 and C2′), which greatly facilitates rRNA maturation. Our structures and specific pre-rRNA cleavage findings provide crucial insights into the mechanism and pathway of pre-rRNA processing in ribosome biosynthesis.

Introduction

Ribosomes are large molecular machines assembled from numerous proteins and RNAs that are responsible for protein synthesis in cells (Anger et al., 2013; Gasse, Flemming, & Hurt, 2015; Khatter, Myasnikov, Natchiar, & Klaholz, 2015). In eukaryotes, ribosome biosynthesis is tightly coupled to cell growth and cell cycle progression and is critical for regulating normal cell size and maintaining cell cycle progression (Castle et al., 2013). Ribosome biosynthesis is an extremely complicated process involving about 200 assembly and processing factors, which are involved in a series of continuous assembly and processing reactions such as ribosome protein folding, modification, assembly, and precursor rRNA (pre-rRNA) processing (Gasse et al., 2015; Lafontaine, 2015; Pillon, Sobhany, Borgnia, Williams, & Stanley, 2017; Wu et al., 2016). Mature ribosomes in yeast *Saccharomyces cerevisiae* contain 79 proteins and four RNAs (25S, 18S, 5.8S, and 5S rRNA) (Doudna & Rath, 2002; Wilson & Doudna Cate, 2012; Woolford & Baserga, 2013). 5S rRNA is transcribed by RNA polymerase III, whereas 25S, 18S and 5.8S rRNA are cotranscribed by RNA polymerase I as a single long precursor (35S pre-rRNA) (Tomecki, Sikorski, & Zakrzewska-Placzek, 2017). Except 25S, 18S and 5.8S rRNA sequences, the 35S pre-rRNA also includes 5′-external transcribed spacer sequence (ETS), 3′-external transcribed spacer sequence, and two internal transcribed spacer sequences (ITS1 and ITS2) (Fromm et al., 2017). ITS1 located between 5.8S and 18S rRNA and ITS2 located between 5.8S and 25S rRNA (Coleman, 2003; Cote, Greer, & Peculis, 2002). The mature rRNAs are generated by a large number of endonucleases and exonucleases that remove these transcribed spacers step by step through multiple efficient and correct processing reactions (Granneman, Petfalski, & Tollervey, 2011). The pre-rRNA processing factors synergistically produce mature rRNAs and lead to an accurate and efficient assembly of mature ribosome in the nucleolus, which

are key to cell survival (Pillon & Stanley, 2018). Mutations in the genes that encode these pre-rRNA processing factors are often lethal (Tomecki et al., 2017). Although numerous evolutionarily conserved protein factors have been found to be involved in the processing and modification of ribosomal RNA, the detailed pathways of these factors and their specific processing mechanisms are not well understood.

Las1 and Grc3 are highly conserved proteins and have recently been identified as core enzymes involved in processing and removing ITS2 spacer, which is a key step in the synthesis of 60S ribosomal subunit (Gasse et al., 2015; Schillewaert, Wacheul, Lhomme, & Lafontaine, 2012). Las1 is characterized as a nucleolar protein essential for ribosome biogenesis, as well as cell proliferation and cell viability in *Saccharomyces cerevisiae* (Castle, Cassimere, & Denicourt, 2012; Castle, Cassimere, Lee, & Denicourt, 2010; Doseff & Arndt, 1995). It is important to determine the role of Las1 in rRNA metabolic pathways and regulatory networks associated with ribosome biogenesis and cell proliferation. Recent studies have demonstrated that Las1 is an endoribonuclease that contains a HEPN (higher eukaryote and prokaryote nucleotide binding) domain responsible for rRNA processing (Pillon et al., 2020; Pillon et al., 2017). The HEPN domain must be dimerized to form an active nuclease, such as the Cas13 effectors in CRISPR immune defense systems, whose catalytic site is formed by two HEPN domains involved in non-specific cleavage of single-stranded RNA (Knott et al., 2017; Liu, Li, Ma, et al., 2017; Liu, Li, Wang, et al., 2017; Zhang et al., 2018). Interestingly, Las1 specifically cleaves at the C2 site within ITS2 and generates the 7S pre-rRNA and 26S pre-rRNA (Fernandez-Pevida, Kressler, & de la Cruz, 2015). It is not clear why Las1 HEPN nuclease specifically targets and cleaves ITS2 only at C2 site, and whether this cleavage depends on a specific sequence or secondary structure. In addition, the cleavage activity of Las1 is primarily

dependent on another enzyme Grc3. Grc3 is a polynucleotide kinase responsible not only for Las1 nuclease activation, but also for nonspecific phosphorylation of the 5′-OH of the 26S pre-rRNA produced by Las1 cleavage, providing a signal for further processing by Rat1-Rai1 exonuclease (Gordon, Pillon, & Stanley, 2019; Xiang et al., 2009). Although Cryo-EM reveals cross-linked *Chaetomium thermophilum* Las1 and Grc3 assemble into a super-dimer, due to flexibility, critical structural information is missing for the coiled coil (CC) domain of Las1 and the N-terminal and C-terminal regions of Grc3 (Pillon et al., 2019). It remains unknown how Las1 and Grc3 coordinate with each other in terms of substrate binding and nuclease activation.

In this study, we identified that *S. cerevisiae* (Sc) Las1 endoribonuclease initially cleaves ITS2 in a step-by-step fashion at two specific sites, which greatly promotes the maturation of 25S rRNA. Additionally, we solved the crystal structures of full-length ScLas1-Grc3 complex and *Cyberlindnera jadinii* (Cj) Las1-Grc3 complex, as well as the high resolution structure of CjLas1 HEPN domain. Our structural and biochemical findings uncovered a detailed mechanism of polynucleotide kinase-mediated activation of HEPN nuclease, providing a molecular basis for clearly understanding the process of pre-rRNA processing and maturation in ribosome biosynthesis.

Results

Las1 cleaves ITS2 at two specific sites

HEPN endoribonucleases such as Cas13, Ire1, and RNase L are metal-independent RNA specific enzymes that efficiently cleave substrate RNA at multiple sites (Abudayyeh et al., 2016; Huang et al., 2014; Korennykh et al., 2009; Lee et al., 2008; Wang et al., 2014). Las1 is also identified as a HEPN-containing RNase, but it has only been found to initially cut ITS2 RNA at a single specific position (C2). To investigate whether there are other potential

121 sites for Las1 cleavage in ITS2, we performed *in vitro* RNA cleavage assays
122 using a 5′-Cy5- and 3′-Cy3-labeled 33-nt ITS2 RNA substrate (Figure 1A).
123 Las1 shows weak or no detectable activity to ITS2 in the absence of Grc3, but
124 exhibits robust activity in the presence of Grc3 (Figure 1B, Figure 1–figure
125 supplement 1), revealing Grc3-dependent Las1 nuclease activation.
126 Interesting, we observed a single 5′-Cy5-labeled cleavage product, and two
127 prominent 3′-Cy3-labeled cleavage products including a final product and an
128 intermediate product (Figure 1B), suggesting that cleavage of ITS2 substrate
129 occurs at two specific sites. The 33-nt ITS2 substrate RNA harbors the C2 site,
130 which is located between nucleotides A140 and G141 (Figure 1A). In addition
131 to the C2 site, there is another specific position in ITS2 that is able to be
132 processed by Las1. ScLas1 cleaves the 33-nt ITS2 at C2 site to theoretically
133 generate a 10-nt 5′-terminal product and a 23-nt 3′-terminal product (Figure
134 1A). Our merger data shows that the final 5′-terminal and 3′-terminal product
135 bands are at nearly the same horizontal position on the gel (Figure 1B),
136 indicating that they are similar in size. Therefore, we hypothesize that the 23-nt
137 3′-terminal product is an intermediate that can be further processed by Las1 at
138 a specific site to produce two small products. We then mapped the cleavage
139 products using the 33-nt ITS2 RNA without 5′-Cy5- and 3′-Cy3-label. We
140 observed four cleavage bands of approximately 23-nt (P2), 14-nt (P3), 10-nt
141 (P1), and 9-nt (P4) in length (Figure 1C). The 23-nt product (P2) is obviously
142 an intermediate cleavage product, which is further cleaved to generate 14-nt
143 and 9-nt products. Based on these observations, we identify that another
144 cleavage site, which we designated as C2′, is located between nucleotides
145 G154 and C155. Las1 is able to process ITS2 at C2 and C2′ sites in a
146 step-by-step manner, resulting in a 9-nt 3′-end product and a 10-nt 5′-end
147 product.

148 We obtained similar cleavage results with a longer 81-nt ITS2 RNA substrate

149 (Figure 1D, E). To further confirm the cleavage site of C2′, we then mapped the
150 cleavage sites of the 81-nt ITS2 using reverse transcription coupling
151 sequencing methods (Figure 1F). We used an adaptor RNA to separately link
152 the product RNA fragments to form template RNAs. After reverse transcription
153 and sequencing of these template RNAs, we obtained the accurate sequence
154 information for products P2 and P4, revealing that the C2 site is located
155 between nucleotides A140 and G141, and the C2′ site is located between
156 nucleotides G154 and C155.

157 The cleavage products P2, P3, and P4 are all phosphorylated by Grc3, as
158 they all show a slight shift when in the presence of ATP in the reaction (Figure
159 1G). This indicates that Las1 generates 5′-OH terminus following both C2 and
160 C2′ cleavage. The phosphorylated products are further degraded by Rat1-Rai1
161 exonuclease, especially P1 and P2, which are completely degraded under
162 given experimental conditions (Figure 1H).

163 In addition, Grc3 shows no cleavage activity to ITS2 (Figure 1–figure
164 supplement 2), and mutations in the HEPN catalytic residues of Las1 abolish
165 C2 and C2′ cleavage (Figure 1–figure supplement 3), further confirming that
166 both C2 and C2′ cleavages are attributed to metal-independent Las1 RNase
167 (Figure 1–figure supplement 4).

168 **Overall structures of ScLas1-Grc3 complex and CjLas1-Grc3 complex**

169 To elucidate how Las1 and Grc3 cooperate to direct ITS2 cleavage and
170 phosphorylation, we determined the cryo-electron microscopy (cryo-EM) and
171 crystal structures of full-length ScLas1-Grc3 complex at 3.07 Å and 3.69 Å
172 resolution (Figure 2, Figure 2–figure supplement 1, Table 1 and Table 2),
173 respectively. Cleavage assay indicates that ScGrc3 can activate ScLas1
174 nuclease well for ITS2 cleavage, while CjGrc3 exhibits relatively weak

175 activation ability for CjLas1 nuclease (Figure 1B, Figure 1–figure supplement
176 1). To better understand the differences in the mechanisms of Grc3 activation
177 of Las1 between different species, we also solved the cryo-EM and crystal
178 structures of full-length CjLas1-Grc3 complex at 3.39 Å and 3.39 Å resolution
179 (Figure 3, Figure 3–figure supplement 1, Table 1 and Table 2), respectively. To
180 be noted, the crystal structures were solved by molecular replacement method
181 with the cryo-EM maps of Las1-Grc3 complexes. Since the crystal structures
182 have similar quality and resolve more structural information than the cryo-EM
183 structures (Figure 3–figure supplement 2), the subsequent presentations and
184 descriptions are based on the crystal structures.

185 Both structures reveal that Las1 and Grc3 assemble into a tetramer with two
186 copies of each (Figure 2B, C and Figure 3B, C). The architecture of Las1-Grc3
187 tetramer complex resembles a butterfly with outstretched wings. Las1 consists
188 of a relatively conserved N-terminal HEPN domain, a poorly conserved central
189 coiled coil (CC) domain, and a short C-terminal tail motif (LCT) (Figure 2A,
190 Figure 3A, Figure 3–figure supplement 3). Grc3 is composed of an N-terminal
191 domain (NTD), a central polynucleotide kinase (PNK) domain, a C-terminal
192 domain (CTD), and a short C-terminal loop motif (GCT). Two HEPN domains
193 from two Las1 copies are tightly symmetrically stacked together to form a
194 HEPN dimer that constructs the body of the butterfly (Figure 2B and Figure 3B).
195 Two CC domains of Las1 and two Grc3 copies assemble into the left and right
196 wings. The NTD and PNK domains of Grc3 constitute the forewing, while the
197 CTD domain of Grc3 and the CC domain of Las1 form the hindwing. All
198 domains are perfectly stacked together to build a compact and stable tetramer
199 architecture (Figure 2C and Figure 3C). Two Grc3 molecules are assembled
200 on both sides of Las1 HEPN domains to stabilize the conformation of HEPN
201 dimer. The CC domain is located on one side of Grc3 and forms a
202 sandwich-shaped structure with the Grc3 and HEPN domains (Figure 2B and

203 Figure 3B), resulting in Grc3 being anchored by the CC and HEPN domains. In
204 addition, the CTD of Grc3 and the HEPN domain of Las1 tightly grasp Las1
205 LCT and Grc3 GCT, respectively, making Las1-Grc3 tetramer assembly more
206 stable.

207 **Las1 CC domain contributes to ITS2 binding and enhances cutting**

208 In order to explore whether there are structural differences between
209 ScLas1-Grc3 and CjLas1-Grc3 complexes, we conducted structural
210 comparison by superposition the structures of the two complexes. Structural
211 superposition shows that the conformations of all Grc3 domains and Las1
212 HEPN domains are almost identical in the two complexes, while the
213 conformations of Las1 CC domains are significantly different (Figure 4A).

214 Dali server reveals that CC domain shares little structural similarity with any
215 known proteins (Holm & Rosenstrom, 2010). CC domain is mainly composed
216 of α helices and is the largest domain of Las1 (Figure 4B), with low sequence
217 similarity among different species (Figure 3–figure supplement 3), yet its
218 function remains unknown. To determine whether it plays a role in Las1
219 catalyzing ITS2 cleavage, we performed EMSA and *in vitro* RNA cleavage
220 assays using Las1 proteins with or without CC domain truncations. Our data
221 shows that the CC domain contributes to the binding of ITS2 RNA and then
222 facilitates ITS2 cleavage (Figure 4C, D), suggesting that the CC domain may
223 play a role of ITS2 stabilization in the Las1 cutting reaction.

224 **Grc3 GCT binds to the HEPN active center and mediates Las1 activation**

225 The ScLas1-Grc3 tetramer structure shows that two Grc3 GCT are stabilized
226 by two HEPN domains of Las1 (Figure 2). Each Grc3 GCT binds to a groove in
227 each Las1 HEPN domain and extends to the ribonuclease active center
228 (Figure 5A), which is formed by the two HEPN domains via dimerization. The

229 conserved catalytic residues Arg129, His130, His134 with two copies from two
230 HEPN domains form a symmetric catalytic active pocket (Figure 5B). The two
231 C-terminals of Grc3 GCTs tightly bind to the catalytic active pocket through
232 packing and hydrogen bond interactions. Specifically, the side chain of Trp617
233 within Grc3 GCT inserts into the active pocket and forms packing and
234 hydrogen bond with catalytic residue Arg129 (Figure 5B). Moreover, Trp617
235 and His615 in Grc3 form extensive hydrogen bond with residues Arg136,
236 Leu99, Gly98 and His54 within Las1. The Trp617 residue is highly conserved
237 in Grc3 (Figure 5C), and its mutation completely abolishes the ITS2 cleavage
238 (Figure 5D), but has little effect on Las1 binding (Figure 5E), revealing that it
239 plays a crucial role in the activation of HEPN endonuclease. We also mutated
240 each of the residues at the C-terminal of Grc3 and examined the nuclease
241 activity of Las1 complexes with these mutants. Our data shows that alanine
242 substitution of multiply conserved residues dramatically reduces the ITS2
243 cleavage (Figure 5F, Figure 5—figure supplement 1), indicating that these
244 residues are also essential for coordinating Las1 HEPN endonuclease
245 activation.

246 **Las1 LCT drives Las1-Grc3 complex assembly**

247 Our structure exhibits that the Las1 LCT is located in a groove in the CTD
248 domain of Grc3 (Figure 6A). Structure analysis reveals that the Las1 LCT is
249 stabilized by the Grc3 CTD through extensive hydrophobic interactions and
250 hydrogen bonding. The side chains of Trp488, Trp494 and Phe499 of Las1
251 LCT are inserted into the three hydrophobic core regions of Grc3 CTD and
252 form stable hydrophobic interactions with multitudinous hydrophobic residues
253 of Grc3 (Figure 6B, C). Additionally, the side chain of Asn487 and the main
254 chains of Lys497 and Ser489 of Las1 LCT form multiple hydrogen bonds with
255 the sides of Trp573, His543 and the main side of Gln468 of Grc3 (Figure 6B,
256 C). Mutations and deletions of Las1 LCT reduce the enzyme activity of Las1

257 (Figure 6—figure supplement 1). LCT deletions also significantly affect the
258 association between Las1 and Grc3 (Figure 6—figure supplement 2). These
259 results highlight the functional significance of the sequence-dependent
260 recognition of Las1 LCT by Grc3 CTD.

261 **Special crystal structure of Las1 HEPN domain**

262 The biochemical data shows that Las1 exhibits very weak ability to cut ITS2
263 RNA at both C2 and C2′ sites in the absence of Grc3 (Figure 1B, Figure
264 1—figure supplement 1), suggesting that Las1 may exist in a low-activity
265 conformation state prior to assembly with Grc3 (Pillon et al., 2017). To
266 determine the structure of Las1 in the low-activity conformation, we screened a
267 lot of crystallization conditions with full-length Las1 proteins. Unfortunately, we
268 did not obtain any crystals. We conjectured that the CC domain of Las1 might
269 have a flexible conformation in the absence of Grc3, and then attempted to
270 crystallize Las1 truncated by the CC domain and LCT. After screening a large
271 number of crystallization conditions, we successfully obtained well-ordered
272 crystals of the CjLas1 HEPN domain and determined its structure at 1.80 Å
273 resolution using molecular replacement method (Figure 7A and Table 1).

274 The crystallographic asymmetric unit contained three Las1 HEPN molecules
275 (HEPN1, HEPN2 and HEPN3), each of which assumes an all α-helical fold
276 (Figure 7A). Analysis of crystal packing and interactions across HEPN-HEPN
277 interfaces suggests that the biological unit of Las1 HEPN domain may contain
278 a homodimer and a monomer. HEPN1 and HEPN2 molecules form a face to
279 face dimer related through the preudo-2-fold axis, similar to the HEPN dimer in
280 the Las1-Grc3 tetramer structure. Most notably, the molecule HEPN3 is likely
281 not to form a dimer similar to HEPN1-HEPN2 with its symmetry-related
282 molecule. Firstly, the structural superposition of HEPN3 and its
283 symmetry-related molecule with the HEPN1-HEPN2 dimer shows that HEPN1

284 and HEPN3 molecules superimpose well with core root mean-square deviation
285 (RMSD) of 0.7 Å for 133 Cα atoms, while HEPN2 and symmetry-related
286 HEPN3 molecule exhibit significantly different conformations (Figure 7—figure
287 supplement 1). Secondly, the catalytic residues in HEPN1 and HEPN2
288 domains are close to each other to form a compact active center, whereas the
289 catalytic residues in HEPN3 and its symmetry-related molecule remain far
290 apart, presenting two separate catalytic sites (Figure 7B, C). These
291 observations suggest that the HEPN3 molecule in the asymmetric unit is
292 probably to be a monomer, which forms a special packing with the dimer of
293 HEPN1-HEPN2 in the crystal.

294 Together, these results indicate a monomer-dimer equilibrium in the Las1
295 HEPN domain, which is consistent with the previously reported SEC-MALS
296 data (Pillon et al., 2017).

297 **Conformational changes in Las1 HEPN domain upon Grc3 binding**

298 Since Grc3 binding significantly activates the endonuclease activity of Las1,
299 the HEPN nuclease domains are probably to undergo conformational changes
300 before and after Grc3 binding. We compared the HEPN domain dimer
301 structures in CjLas1 and CjLas1-Grc3 complex by superposition and observed
302 that significant conformational changes occur in HEPN domains upon Grc3
303 binding (Figure 7D). One HEPN domain is well aligned between the two
304 structures, while the other HEPN domain has a large displacement. In order to
305 investigate whether conformational changes occurred in the catalytic center,
306 we further compared the catalytic pocket within the HEPN domains of the two
307 structures. Remarkably, Large conformational changes are observed in the
308 catalytic pocket (Figure 7D). In the Grc3-free Las1 structure, the catalytic
309 residues Arg129, His130 and His134 within one HEPN domain are far from the
310 catalytic residues in the other HEPN domain, while in the Grc3-bound structure,

311 the catalytic residues within two HEPN domains are close to each other
312 (Figure 7D, Figure 7—figure supplement 2). These observations indicate that
313 the Grc3 binding not only stabilizes the Las1 HEPN dimer, but also promotes
314 the formation of a more compact catalytic pocket, showing better catalytic
315 activity for specific cleavage of ITS2. Notably, compared with CjGrc3-bound
316 CjLas1, ScGrc3-bound ScLas1 has a more compact catalytic pocket (Figure
317 7D, Figure 7—figure supplement 2), which may explain why ScLas1 shows
318 better ITS2 cleavage activity than CjLas1 in the presence of Grc3 (Figure 1B,
319 Figure 1—figure supplement 1).

320 **Discussion**

321 Removal of the ITS2 is the requirement for the maturation of 5.8S rRNA and
322 25S rRNA, which is an important step during the eukaryotic 60S subunit
323 synthesis. In this study, the structural, biochemical, and functional analysis of
324 ITS2 RNA processing machinery provides a critical step toward understanding
325 the molecular mechanism of Grc3-activated ITS2 processing by Las1
326 endoribonuclease.

327 **Mechanism of ITS2 processing by Las1-Grc3 dual enzyme complex**

328 Based on our findings, we propose a model of ITS2 processing by Las1
329 endoribonuclease and its activator Grc3 kinase (Figure 8). In the absence of
330 Grc3, Las1 has very weak ITS2 cleavage activity due to its unstable HEPN
331 dimer. However, in the presence of Grc3, two copies of Las1 and Grc3
332 assemble into a stable tetramer that shows high activity to cleavage ITS2.
333 Las1 initially processes ITS2 at the C2 site, generating a 5.8S rRNA precursor
334 with 2′,3′-cyclic phosphate and a 25S rRNA precursor with 5′-hydroxyl end
335 (Figure 8 and Figure 1I). The second step of ITS2 specific cleavage occurs at
336 the C2′ site to remove the 5′-region of the 25S rRNA precursor. The C2′

337 cleavage also produces a 5′-hydroxyl product, which is rapidly phosphorylated
338 by Grc3 only in the presence of ATP. After phosphorylation, the 25S precursor
339 is further processed by a Rat1-Rai1 complex with 5′−3′ exonuclease activity,
340 which degrades the 5′-region of the 25S rRNA precursor and subsequently
341 generate mature 25S rRNA (Figure 1I) (Gasse et al., 2015). Furthermore, the
342 nuclear exosome complex drives the maturation of the 5.8S RNA by removing
343 the 3′-end of the precursor through its 3′−5′ exonuclease activity (Fromm et al.,
344 2017).

345 **Distinct activation mechanism for Las1 HEPN nuclease**

346 Structural and biochemical results highlight the mechanism of Grc3
347 GCT-mediated Las1 HEPN nuclease activation, which is quite distinct from
348 other HEPN nucleases such as CRISPR-Cas and toxin-antitoxin associated
349 HEPN RNases, Cas13a, Csm6, RnlA. Though proper dimerization of the
350 HEPN domain is critical for HEPN nuclease activity, other factors are also
351 common requirements for HEPN activation. For examples, activation of the
352 Cas13a HEPN enzyme requires target RNA binding and guide-target RNA
353 duplex formation, while allosterically activation of the Csm6 HEPN nuclease is
354 dependent on a cyclic oligoadenylate (Liu, Li, Ma, et al., 2017; Niewoehner et
355 al., 2017). In addition, stimulating the toxicity of RnlA HEPN RNase requires an
356 association between RnlA and RNase HI, and trigging activation of the HEPN
357 domains of Ire1 and RNase L needs binding of ATP to their kinase domains
358 (Lee et al., 2008; Naka, Koga, Yonesaki, & Otsuka, 2014; Wang et al., 2014). It
359 is noteworthy that these activators do not interact directly with the HEPN
360 domain, but bind to other domains to induce a conformational transition of the
361 HEPN domain from inactive to active state. In contrast, Grc3 GCTs bind
362 directly to the active center of HEPN domains and form hydrogen bonds with
363 catalytic residues, which appears to provoke rearrangements of the active site
364 required for activation of HEPN. Regulation of HEPN RNases by interacting

with catalytic residues may be a direct and effective measure.

Comparison of Las1-Grc3 complex and other nuclease-kinase machines

Ire1 and RNase L are also nuclease-kinase machines that contain a HEPN domain and a protein kinase domain or a pseudo-protein kinase domain, playing a fundamental role in RNA degradation related to a variety of cellular processes. Although Ire1 and RNase L also require higher-order assembly during RNA degradation, the Las1-Grc3 complex shows distinct structure assembly with them (Figure 8—figure supplement 1). Both the kinase domain and the HEPN domain in Ire1 and RNase L adopt a parallel back to back dimer configuration (Lee et al., 2008; Wang et al., 2014). In Las1, only the HEPN domain forms a dimer architecture, and Grc3 does not contact each other, but binds on both sides to stabilize the HEPN dimer. An ankyrin repeat domain in RNase L and an endoplasmic reticulum (ER) luminal domain in Ire1 has been proposed to promote dimerization of the kinase and HEPN domains (Credle, Finer-Moore, Papa, Stroud, & Walter, 2005; Huang et al., 2014). Whereas the additional CC domain in Las1 is likely to contribute to RNA binding and facilitate cleavage (Figure 4C, D). In addition, Las1, Ire1, and RNase L recognize similar RNA cleavage motifs despite being involved in different RNA processing, splicing, and degradation pathways. Cleavage studies show a preference of Las1 for UAG and UGC motifs, which are also the universal cleavage motifs observed in mRNA decay by Ire1 and RNase L (Pillon & Stanley, 2018).

Materials and methods

Protein expression and purification

For Las1-Grc3 complex expression and purification, *Saccharomyces*

391 *cerevisiae Las1* (*ScLas1*) *gene* was cloned into pET23a vector with an
392 N-terminal His_6-tag and *Cyberlindnera jadinii* (*CjLas1*) gene was cloned into
393 pET28a vector with an N-terminal His_6SUMO-tag, while *ScGrc3* and *CjGrc3*
394 genes were cloned into modified pET28a vector containing an N-terminal
395 SUMO-tag, followed by an ubiquitin-like protein1 (Ulp1) protease cleavage site.
396 All recombinant plasmids were transformed into *E.coli* Rosetta (DE3)
397 (Novagen) cells and grown in LB broth at 37°C for 3 h. After culturing to an
398 OD_{600} of 0.6-0.8, protein expression was induced with 0.2 mM
399 isopropyl-1-thio-β-D-galactopyranoside (IPTG) at 16°C for 14 h. For the
400 purification of ScLas1-Grc3 complex proteins, cells expressing ScLas1
401 proteins and ScGrc3 proteins were collected and co-lysed by sonication in
402 buffer containing 20 mM Tris-HCl, pH 7.5, 500 mM NaCl. After centrifugation,
403 supernatant was incubated with Ni Sepharose (GE Healthcare), and the bound
404 protein was eluted with buffer containing 20 mM Tris-HCl, pH 7.5, 300 mM
405 NaCl, 300 mM imidazole. Eluted protein was digested with Ulp1 protease at
406 4°C for 2 h and then further purified on a Heparin HP column (GE Healthcare),
407 eluting with a linear gradient of increasing NaCl concentration from 300 mM to
408 1 M in 20 mM Tris-HCl, pH7.5 buffer. The fractions containing the protein of
409 interest were concentrated and further purified by size-exclusion
410 chromatography (Superdex 200 Increase 10/300, GE Healthcare) in a buffer
411 containing 20 mM Tris-HCl, pH 7.5, 300 mM NaCl, and 1 mM
412 Tris(2-carboxyethyl)phosphine hydrochloride (TCEP). Proteins were collected
413 and concentrated to a final concentration of 15 mg/ml. For the purification of
414 CjLas1-Grc3 complex proteins, cells expressing CjLas1 proteins and CjGrc3
415 proteins were collected and co-lysed by sonication in buffer containing 20 mM
416 Tris-HCl, pH 7.5, 500 mM NaCl. After centrifugation, supernatant was
417 incubated with Ni Sepharose (GE Healthcare), and the bound protein was
418 eluted with buffer containing 20 mM Tris-HCl, pH 7.5, 350 mM NaCl, 300 mM
419 imidazole. Eluted protein was digested with Ulp1 protease at 4°C for 2 h and

420 then further purified on a Heparin HP column (GE Healthcare), eluting with
421 buffer containing 20 mM Tris-HCl, pH7.5, 1M NaCl. The protein was further
422 purified by size-exclusion chromatography (Superdex 200 Increase 10/300,
423 GE Healthcare) in a buffer containing 20 mM Tris-HCl, pH 7.5, 350 mM NaCl,
424 and 1 mM Tris(2-carboxyethyl)phosphine hydrochloride (TCEP). Proteins were
425 collected and concentrated to a final concentration of 15 mg/ml. Mutants were
426 expressed and purified as wild-type protein. The CjLas1 HEPN construct was
427 purified with an identical protocol.

428 For the experiment of GST pull-down, the wild-type *ScLas1* gene and its
429 mutants were cloned into a modified pET23a vector (Novagen) with an
430 N-terminal His_6GST-tag, while the wild-type *ScGrc3* gene and its mutants were
431 cloned into a modified pET28a vector containing an N-terminal His_6SUMO-tag.
432 Proteins were overexpressed in *E.coli* Rosetta (DE3) (Novagen) cells and
433 cultured in LB broth to an OD_{600} of 0.6-0.8. Then the target proteins were
434 induced with 0.2 mM isopropyl-1-thio-β-D-galactopyranoside (IPTG) and
435 grown for additional 14 h at 16°C. Cells were collected and lysed by sonication
436 in buffer containing 20 mM Tris-HCl, pH 7.5, 500 mM NaCl. After centrifugation,
437 supernatant was incubated with Ni Sepharose (GE Healthcare), and the bound
438 protein was eluted with buffer containing 20 mM Tris-HCl, pH 7.5, 300 mM
439 NaCl, 300 mM imidazole. The GST-ScLas1 mutants were further purified on a
440 Heparin HP column (GE Healthcare) and ScGrc3 mutants were purified on a
441 HitTrap Q HP column (GE Healthcare). All proteins were further purified by
442 size-exclusion chromatography (Superdex 200 Increase 10/300, GE
443 Healthcare) in a buffer containing 20 mM Tris-HCl, pH 7.5, 300 mM NaCl.

444 **Crystallization, data collection and structure determination**

445 Crystals of ScLas1-Grc3 complex, CjLas1-Grc3 complex and CjLas1 truncated
446 protein (HEPN domain) were first obtained using the sitting drop vapor
447 diffusion method using high-throughput crystallization screening kits (Hampton

448 Research, Molecular Dimensions and QIAGEN). Crystals were then grown in a
449 mixed solution containing 1 μl complex solution and 1 μl of reservoir solution
450 using the hanging drop vapor diffusion method at 16°C. For growing large
451 crystals, crystals were further optimized by using seeding technique.
452 Well-diffracting crystals of ScLas1-Grc3 complex were grown in a reservoir
453 solution containing 2% (v/v) tacsimate, pH 7.0, 0.1 M imidazole, pH 7.0, 2%
454 (v/v) 2-propanol, and 9% (w/v) PEG 3350. Well-diffracting crystals of
455 CjLas1-Grc3 complex were grown in a reservoir solution containing 0.1 M
456 sodium phosphate, pH 7.5, 0.05 M NaCl, and 9% (w/v) PEG 4000. The best
457 crystals of CjLas1 HEPN domain protein were grown from 0.1 M Tris-HCl, pH
458 8.0, 0.2 M $MgCl_2$, and 25% (w/v) PEG 3350. All crystals soaked in
459 cryoprotectants made from the mother liquors supplemented with 20% (v/v)
460 glycerol and flash frozen in liquid nitrogen.

461 All diffraction data sets were collected at beamline BL-17U1, BL-18U1, and
462 BL-19U1 at Shanghai Synchrotron Radiation Facility (SSRF) and National
463 Center for Protein Sciences Shanghai (NCPSS), and processed with HKL3000
464 (Otwinowski & Minor, 1997). The CjLas1 HEPN structure were determined by
465 molecular replacement using the HEPN domain structure within CtLas1-Grc3
466 (PDB: 6OF4) as the search model using the program PHENIX Phaser (Adams
467 et al., 2002; Pillon et al., 2019). The phases of ScLas1-Grc3 complex and
468 CjLas1-Grc3 complex were solved by molecular replacement method with the
469 cryo-EM maps of Las1-Grc3 complexes using PHENIX Phaser. The model
470 was manually built and adjusted using the program COOT (Emsley, Lohkamp,
471 Scott, & Cowtan, 2010). Iterative cycles of crystallographic refinement were
472 performed using PHENIX. All data processing and structure refinement
473 statistics are summarized in Supplementary Table 1. Structure figures were
474 prepared using PyMOL (http://www.pymol.org/).

475 **Cryo-EM data acquisition**

476 The samples were diluted at a final concentration of around 1.0 mg/mL. Three
477 microliters of the samples were applied onto glow-discharged 200-mesh R2/1
478 Quantifoil copper grids. The grids were blotted for 4 s and rapidly cryocooled in
479 liquid ethane using a Vitrobot Mark IV (Thermo Fisher Scientific) at 4°C and
480 100% humidity. The samples were imaged in a Titan Krios cryo-electron
481 microscope (Thermo Fisher Scientific) at a magnification of 105,000×
482 (corresponding to a calibrated sampling of 0.82 Å per pixel). Micrographs were
483 recorded by EPU software (Thermo Fisher Scientific) with a K3 detector, where
484 each image was composed of 30 individual frames an exposure time of 3 s
485 and an exposure rate of 16.7 electrons per second per $Å^2$. A total of 2,520
486 movie stacks for ScLas1-Grc3 complex and 8,616 movie stacks for
487 CjLas1-Grc3 complex were collected.

488 **Single-particle image processing and 3D reconstruction**

489 All micrographs were first imported into Relion (Scheres, 2012) for image
490 processing. The motion-correction was performed using MotionCor2 (Zheng et
491 al., 2017) and the contrast transfer function (CTF) was determined using
492 CTFFIND4 (Rohou & Grigorieff, 2015). All particles were autopicked using the
493 NeuralNet option in EMAN2 (Tang et al., 2007). Then, particle coordinates
494 were imported to Relion, where the poor 2D class averages were removed by
495 several rounds of 2D classification. Initial maps were built and classified using
496 ab-initio 3D reconstruction in cryoSPARC (Punjani, Rubinstein, Fleet, &
497 Brubaker, 2017) without any symmetry applied. Heterogeneous refinement
498 was further performed to remove bad particles using one good and one bad
499 starting maps. The good class having 264,341 particles for ScLas1-Grc3
500 complex or 523,843 particles for CjLas1-Grc3 complex was selected and
501 subjected to 3D homogeneous refinement, local & global CTF refinement, and
502 non-uniform refinement with C2 symmetry imposed, achieving a 3.07 Å
503 resolution map for the ScLas1-Grc3 complex and a 3.39 Å resolution map for
504 the CjLas1-Grc3 complex, respectively. Resolution for the final maps were

505 estimated with the 0.143 criterion of the Fourier shell correlation curve.
506 Resolution maps were calculated in cryoSPARC using the "Local Resolution
507 Estimation" option. (More information in Supplementary Figure S2,
508 Supplementary Figure S3, and Supplementary Table 2).

509 ***In vitro* transcription of RNA**

510 Unlabeled ITS2 RNAs used for cleavage assays were synthesized by *in vitro*
511 transcription with T7 RNA polymerase and linearized plasmid DNAs as
512 templates. Transcription reactions were performed at 37°C for 4 h in buffer
513 containing 100 mM HEPES-KOH, pH 7.9, 20 mM $MgCl_2$, 30 mM DTT, 2 mM
514 each NTP, 2 mM spermidine, 0.1 mg/ml T7 RNA polymerase, and 40 ng/μl
515 linearized plasmid DNA template. The transcribed RNA was then purified by
516 gel electrophoresis on a 12% denaturing (8 M urea) polyacrylamide gel, RNA
517 band was excised from the gel and recovered with Elutrap System. The
518 purified RNA was resuspended in DEPC (diethy pyrocarbonate)-treated water.

519 ***In vitro* ITS2 RNA cleavage assays**

520 For 5′-Cy5 and 3′-Cy3 labeled ITS2 RNA cleavage assays, 0.5 μM of ITS2
521 RNA was incubated at 37°C for 2 h with increasing amount of Las1, Grc3 or
522 Las1-Grc3 complex proteins (0.05 μM-0.5 μM) in cleavage buffer containing 20
523 mM Tris-HCl, pH 7.5, 300 mM NaCl, 1 mM Tris(2-carboxyethyl)phosphine
524 hydrochloride (TCEP). 5′-Cy5 and 3′-Cy3 labeled ITS2 RNA was synthesized
525 from Takara Biomedical Technology. Reactions were stopped by adding 2 ×
526 loading buffer. Samples were analyzed on a 20% urea denaturing
527 polyacrylamide gel with TBE buffer. Cleavage products were visualized by
528 fluorescent imaging and analysis system (SINSAGE TECHNOLOGY).

529 For unlabeled ITS2 RNA cleavage assays, 10 μM of ITS2 RNA was
530 incubated at 37°C for 2 h with increasing amount of Las1, Grc3 or Las1-Grc3
531 complex proteins (1.5 μM-15 μM) in cleavage buffer containing 20 mM
532 Tris-HCl, pH 7.5, 300 mM NaCl, 1 mM Tris(2-carboxyethyl)phosphine

533 hydrochloride (TCEP). Reactions were stopped by adding 2 × loading buffer
534 and were then quenched at 75°C for 5 min. Samples were analyzed on a 20%
535 urea denaturing polyacrylamide gel with TBE buffer. Cleavage products were
536 visualized by toluidine blue staining.

537 **RNA cleavage products phosphorylation assays**

538 10 μM of unlabeled ITS2 RNA was incubated at 37°C for 1.5 h with 10 μM of
539 Las1-Grc3 complex proteins in cleavage buffer containing 20 mM Tris-HCl, pH
540 7.5, 300 mM NaCl, 1 mM Tris(2-carboxyethyl)phosphine hydrochloride (TCEP).
541 1 mM ATP was added into each reaction system at 37°C for 30 min. Reactions
542 were stopped by adding 2 × loading buffer and were then quenched at 75°C for
543 5 min. Samples were analyzed on a 20% urea denaturing polyacrylamide gel
544 with TBE buffer. Cleavage products were visualized by toluidine blue staining.

545 **GST pull-down assays**

546 Pull-down experiments were carried out using GST fusion proteins to analyze
547 the association between Las1 and Grc3. 0.2 mg purified GST-ScLas1 protein
548 were incubated with 0.4 mg purified ScGrc3 protein in binding buffer containing
549 20 mM Tris-HCl, pH 7.5, 500 mM NaCl, 2 mM DTT. 80 μl GST affinity resin was
550 added into each reaction system at 4°C for 60 min. The resin was washed with
551 1 ml of binding buffer. After washing five times, the binding samples were
552 eluted with elution buffer containing 20 mM Tris, pH 7.5, 20 mM GSH, 500 mM
553 NaCl, and 2 mM DTT. The elution samples were then monitored using
554 SDS-PAGE (polyacrylamide gel electrophoresis) and visualized by Coomassie
555 blue staining. The assays were quantified by band densitometry. The
556 experiment was repeated three times.

557 **Electrophoretic mobility shift assays**

558 Electrophoretic mobility shift assays (EMSA) were performed with a series of
559 Las1-Grc3 complex dilutions from 20 μM to 2 μM and a 81-nt ITS2 RNA. the

560 ITS2 RNA was synthesized by in vitro transcription. Proteins were incubated
561 with ITS2 RNA in a binding buffer containing 20 mM Tris-HCl, pH 7.5, 300 mM
562 NaCl for 30 min at 4°C. After reaction, the binding samples were then resolved
563 on 5% native acrylamide gels in Tris-Glycine (0.5X TBE) buffer pH 8.5 under
564 an electric field of 100 volts for 40 min at 4°C. Gels were imaged by using a
565 ChemiDoc XRS+ (Bio-rad).

566 **RNA sequencing**

567 Enzyme-digested products from the ITS2 cleavage assay were isolated by
568 dialysis from denaturing polyacrylamide gel. T4 PNK was used to
569 phosphorylate the 5′ terminus of RNA products. After the above treatment,
570 RNA samples were linked with the adaptor RNA by T4 RNA ligase-1. RNA
571 samples were then treated for reverse transcription and PCR amplification.
572 The PCR amplification products were cloned into pET28a vector, then
573 sequenced.

574

575 **Data availability**

576 The atomic coordinates included in this study have been deposited in the
577 Protein Data Bank (PDB) with the following accession codes: 7Y16, 7Y17, and
578 7Y18. Cryo-EM maps of the ScLas1-Grc3 complex and CjLas1-Grc3 complex
579 in this study have been deposited in the wwPDB OneDep System under EMD
580 accession code EMD-33733 and EMD-33735.

581 **Acknowledgements**

582 We are grateful to the staff of the BL-17U1, BL-18U1 and BL-19U1 beamlines
583 at the National Center for Protein Sciences Shanghai (NCPSS) at Shanghai
584 Synchrotron Radiation Facility (SSRF).

585 **Author contributions**

586 J.C., H.C., X.L., and R.H. expressed and purified the proteins and grew
587 crystals. J.C., H.C., and L.L. collected X-ray diffraction data. S.L., K.Z., and L.L.
588 solved the structures. X.L., H.C., R.H., and J.C. carried out all of the cloning
589 and performed the biochemical assays. L.L. prepared the figures; L.L. wrote
590 the manuscript and supervised all of the research.

591 **Funding**

592 National Natural Science Foundation of China [32171286].

593 • Liang Liu

594 The funders had no role in study design, data collection and interpretation, or
595 the decision to submit the work for publication.

596 **Competing interests**

597 The authors declare no competing interests.

598

599 **References**

600 Abudayyeh, O. O., Gootenberg, J. S., Konermann, S., Joung, J., Slaymaker, I. M., Cox, D.
601 B., . . . Zhang, F. (2016). C2c2 is a single-component programmable RNA-guided
602 RNA-targeting CRISPR effector. *Science, 353*(6299), aaf5573.
603 doi:10.1126/science.aaf5573

604 Adams, P. D., Grosse-Kunstleve, R. W., Hung, L. W., Ioerger, T. R., McCoy, A. J., Moriarty, N.
605 W., . . . Terwilliger, T. C. (2002). PHENIX: building new software for automated
606 crystallographic structure determination. *Acta Crystallogr D Biol Crystallogr, 58*(Pt 11),
607 1948-1954. doi:10.1107/s0907444902016657

608 Anger, A. M., Armache, J. P., Berninghausen, O., Habeck, M., Subklewe, M., Wilson, D. N., &

609 Beckmann, R. (2013). Structures of the human and Drosophila 80S ribosome. *Nature, 497*(7447), 80-85. doi:10.1038/nature12104

611 Castle, C. D., Cassimere, E. K., & Denicourt, C. (2012). LAS1L interacts with the mammalian Rix1 complex to regulate ribosome biogenesis. *Mol Biol Cell, 23*(4), 716-728. doi:10.1091/mbc.E11-06-0530

614 Castle, C. D., Cassimere, E. K., Lee, J., & Denicourt, C. (2010). Las1L is a nucleolar protein required for cell proliferation and ribosome biogenesis. *Mol Cell Biol, 30*(18), 4404-4414. doi:10.1128/MCB.00358-10

617 Castle, C. D., Sardana, R., Dandekar, V., Borgianini, V., Johnson, A. W., & Denicourt, C. (2013). Las1 interacts with Grc3 polynucleotide kinase and is required for ribosome synthesis in Saccharomyces cerevisiae. *Nucleic Acids Res, 41*(2), 1135-1150. doi:10.1093/nar/gks1086

621 Coleman, A. W. (2003). ITS2 is a double-edged tool for eukaryote evolutionary comparisons. *Trends Genet, 19*(7), 370-375. doi:10.1016/S0168-9525(03)00118-5

623 Cote, C. A., Greer, C. L., & Peculis, B. A. (2002). Dynamic conformational model for the role of ITS2 in pre-rRNA processing in yeast. *RNA, 8*(6), 786-797. doi:10.1017/s1355838202023063

626 Credle, J. J., Finer-Moore, J. S., Papa, F. R., Stroud, R. M., & Walter, P. (2005). On the mechanism of sensing unfolded protein in the endoplasmic reticulum. *Proc Natl Acad Sci U S A, 102*(52), 18773-18784. doi:10.1073/pnas.0509487102

629 Doseff, A. I., & Arndt, K. T. (1995). LAS1 is an essential nuclear protein involved in cell morphogenesis and cell surface growth. *Genetics, 141*(3), 857-871.

631 doi:10.1093/genetics/141.3.857

632 Doudna, J. A., & Rath, V. L. (2002). Structure and function of the eukaryotic ribosome: the next
633 frontier. *Cell, 109*(2), 153-156. doi:10.1016/s0092-8674(02)00725-0

634 Emsley, P., Lohkamp, B., Scott, W. G., & Cowtan, K. (2010). Features and development of
635 Coot. *Acta Crystallogr D Biol Crystallogr, 66*(Pt 4), 486-501.
636 doi:10.1107/S0907444910007493

637 Fernandez-Pevida, A., Kressler, D., & de la Cruz, J. (2015). Processing of preribosomal RNA
638 in Saccharomyces cerevisiae. *Wiley Interdiscip Rev RNA, 6*(2), 191-209.
639 doi:10.1002/wrna.1267

640 Fromm, L., Falk, S., Flemming, D., Schuller, J. M., Thoms, M., Conti, E., & Hurt, E. (2017).
641 Reconstitution of the complete pathway of ITS2 processing at the pre-ribosome. *Nat*
642 *Commun, 8*(1), 1787. doi:10.1038/s41467-017-01786-9

643 Gasse, L., Flemming, D., & Hurt, E. (2015). Coordinated Ribosomal ITS2 RNA Processing by
644 the Las1 Complex Integrating Endonuclease, Polynucleotide Kinase, and
645 Exonuclease Activities. *Mol Cell, 60*(5), 808-815. doi:10.1016/j.molcel.2015.10.021

646 Gordon, J., Pillon, M. C., & Stanley, R. E. (2019). Nol9 Is a Spatial Regulator for the Human
647 ITS2 Pre-rRNA Endonuclease-Kinase Complex. *J Mol Biol, 431*(19), 3771-3786.
648 doi:10.1016/j.jmb.2019.07.007

649 Granneman, S., Petfalski, E., & Tollervey, D. (2011). A cluster of ribosome synthesis factors
650 regulate pre-rRNA folding and 5.8S rRNA maturation by the Rat1 exonuclease. *EMBO*
651 *J, 30*(19), 4006-4019. doi:10.1038/emboj.2011.256

652 Holm, L., & Rosenstrom, P. (2010). Dali server: conservation mapping in 3D. *Nucleic Acids*

Res, 38(Web Server issue), W545-549. doi:10.1093/nar/gkq366

Huang, H., Zeqiraj, E., Dong, B., Jha, B. K., Duffy, N. M., Orlicky, S., . . . Sicheri, F. (2014). Dimeric structure of pseudokinase RNase L bound to 2-5A reveals a basis for interferon-induced antiviral activity. *Mol Cell, 53*(2), 221-234. doi:10.1016/j.molcel.2013.12.025

Khatter, H., Myasnikov, A. G., Natchiar, S. K., & Klaholz, B. P. (2015). Structure of the human 80S ribosome. *Nature, 520*(7549), 640-645. doi:10.1038/nature14427

Knott, G. J., East-Seletsky, A., Cofsky, J. C., Holton, J. M., Charles, E., O'Connell, M. R., & Doudna, J. A. (2017). Guide-bound structures of an RNA-targeting A-cleaving CRISPR-Cas13a enzyme. *Nat Struct Mol Biol, 24*(10), 825-833. doi:10.1038/nsmb.3466

Korennykh, A. V., Egea, P. F., Korostelev, A. A., Finer-Moore, J., Zhang, C., Shokat, K. M., . . . Walter, P. (2009). The unfolded protein response signals through high-order assembly of Ire1. *Nature, 457*(7230), 687-693. doi:10.1038/nature07661

Lafontaine, D. L. (2015). Noncoding RNAs in eukaryotic ribosome biogenesis and function. *Nat Struct Mol Biol, 22*(1), 11-19. doi:10.1038/nsmb.2939

Lee, K. P., Dey, M., Neculai, D., Cao, C., Dever, T. E., & Sicheri, F. (2008). Structure of the dual enzyme Ire1 reveals the basis for catalysis and regulation in nonconventional RNA splicing. *Cell, 132*(1), 89-100. doi:10.1016/j.cell.2007.10.057

Liu, L., Li, X., Ma, J., Li, Z., You, L., Wang, J., . . . Wang, Y. (2017). The Molecular Architecture for RNA-Guided RNA Cleavage by Cas13a. *Cell, 170*(4), 714-726 e710. doi:10.1016/j.cell.2017.06.050

675 Liu, L., Li, X., Wang, J., Wang, M., Chen, P., Yin, M., . . . Wang, Y. (2017). Two Distant
676 Catalytic Sites Are Responsible for C2c2 RNase Activities. *Cell, 168*(1-2), 121-134
677 e112. doi:10.1016/j.cell.2016.12.031
678 Naka, K., Koga, M., Yonesaki, T., & Otsuka, Y. (2014). RNase HI stimulates the activity of
679 RnlA toxin in Escherichia coli. *Mol Microbiol, 91*(3), 596-605. doi:10.1111/mmi.12479
680 Niewoehner, O., Garcia-Doval, C., Rostol, J. T., Berk, C., Schwede, F., Bigler, L., . . . Jinek, M.
681 (2017). Type III CRISPR-Cas systems produce cyclic oligoadenylate second
682 messengers. *Nature, 548*(7669), 543-548. doi:10.1038/nature23467
683 Otwinowski, Z., & Minor, W. (1997). Processing of X-ray diffraction data collected in oscillation
684 mode. *Methods Enzymol, 276*, 307-326.
685 Pillon, M. C., Goslen, K. H., Gordon, J., Wells, M. L., Williams, J. G., & Stanley, R. E. (2020). It
686 takes two (Las1 HEPN endoribonuclease domains) to cut RNA correctly. *J Biol Chem,*
687 *295*(18), 5857-5870. doi:10.1074/jbc.RA119.011193
688 Pillon, M. C., Hsu, A. L., Krahn, J. M., Williams, J. G., Goslen, K. H., Sobhany, M., . . . Stanley,
689 R. E. (2019). Cryo-EM reveals active site coordination within a multienzyme pre-rRNA
690 processing complex. *Nat Struct Mol Biol, 26*(9), 830-839.
691 doi:10.1038/s41594-019-0289-8
692 Pillon, M. C., Sobhany, M., Borgnia, M. J., Williams, J. G., & Stanley, R. E. (2017). Grc3
693 programs the essential endoribonuclease Las1 for specific RNA cleavage. *Proc Natl*
694 *Acad Sci U S A, 114*(28), E5530-E5538. doi:10.1073/pnas.1703133114
695 Pillon, M. C., & Stanley, R. E. (2018). Nuclease integrated kinase super assemblies (NiKs) and
696 their role in RNA processing. *Curr Genet, 64*(1), 183-190.

doi:10.1007/s00294-017-0749-9

Punjani, A., Rubinstein, J. L., Fleet, D. J., & Brubaker, M. A. J. N. m. (2017). cryoSPARC: algorithms for rapid unsupervised cryo-EM structure determination. *14*(3), 290-296.

Rohou, A., & Grigorieff, N. J. J. o. s. b. (2015). CTFFIND4: Fast and accurate defocus estimation from electron micrographs. *192*(2), 216-221.

Scheres, S. H. J. J. o. s. b. (2012). RELION: implementation of a Bayesian approach to cryo-EM structure determination. *180*(3), 519-530.

Schillewaert, S., Wacheul, L., Lhomme, F., & Lafontaine, D. L. (2012). The evolutionarily conserved protein Las1 is required for pre-rRNA processing at both ends of ITS2. *Mol Cell Biol, 32*(2), 430-444. doi:10.1128/MCB.06019-11

Tang, G., Peng, L., Baldwin, P. R., Mann, D. S., Jiang, W., Rees, I., & Ludtke, S. J. J. J. o. s. b. (2007). EMAN2: an extensible image processing suite for electron microscopy. *157*(1), 38-46.

Tomecki, R., Sikorski, P. J., & Zakrzewska-Placzek, M. (2017). Comparison of preribosomal RNA processing pathways in yeast, plant and human cells - focus on coordinated action of endo- and exoribonucleases. *FEBS Lett, 591*(13), 1801-1850. doi:10.1002/1873-3468.12682

Wang, Y., Li, Y., Toth, J. I., Petroski, M. D., Zhang, Z., & Zhao, J. C. (2014). N6-methyladenosine modification destabilizes developmental regulators in embryonic stem cells. *Nat Cell Biol, 16*(2), 191-198. doi:10.1038/ncb2902

Wilson, D. N., & Doudna Cate, J. H. (2012). The structure and function of the eukaryotic ribosome. *Cold Spring Harb Perspect Biol, 4*(5). doi:10.1101/cshperspect.a011536

719 Woolford, J. L., Jr., & Baserga, S. J. (2013). Ribosome biogenesis in the yeast
720 Saccharomyces cerevisiae. *Genetics, 195*(3), 643-681.
721 doi:10.1534/genetics.113.153197
722 Wu, S., Tutuncuoglu, B., Yan, K., Brown, H., Zhang, Y., Tan, D., . . . Gao, N. (2016). Diverse
723 roles of assembly factors revealed by structures of late nuclear pre-60S ribosomes.
724 *Nature, 534*(7605), 133-137. doi:10.1038/nature17942
725 Xiang, S., Cooper-Morgan, A., Jiao, X., Kiledjian, M., Manley, J. L., & Tong, L. (2009).
726 Structure and function of the 5'-->3' exoribonuclease Rat1 and its activating partner
727 Rai1. *Nature, 458*(7239), 784-788. doi:10.1038/nature07731
728 Zhang, C., Konermann, S., Brideau, N. J., Lotfy, P., Wu, X., Novick, S. J., . . . Lyumkis, D.
729 (2018). Structural Basis for the RNA-Guided Ribonuclease Activity of
730 CRISPR-Cas13d. *Cell, 175*(1), 212-223 e217. doi:10.1016/j.cell.2018.09.001
731 Zheng, S. Q., Palovcak, E., Armache, J.-P., Verba, K. A., Cheng, Y., & Agard, D. A. J. N. m.
732 (2017). MotionCor2: anisotropic correction of beam-induced motion for improved
733 cryo-electron microscopy. *14*(4), 331-332.

734

735 **Figure Legends**

736 **Figure 1. ScLas1 specifically cleaves ITS2 at C2 and C2′ sites. (A)** 33-nt
737 ITS2 RNA with 5′-Cy5 and 3′-Cy3 labels. **(B)** *In vitro* RNA cleavage assay
738 using 5′-Cy5 and 3′-Cy3 labeled 33-nt RNA. **(C)** *In vitro* RNA cleavage assay of
739 unlabeled 33-nt RNA. **(D)** 81-nt ITS2 RNA. **(E)** *In vitro* RNA cleavage assay of
740 unlabeled 81-nt RNA. **(F)** RNA-sequencing traces from ScLas1-cleaved ITS2

741 products P2 and P4. **(G)** RNA phosphorylation assay with ScLas1-Grc3
742 complex. **(H)** RNA degradation assay with ScRat1-Rai1 complex. **(I)** The ITS2
743 pre-rRNA processing pathway.

744 The following figure supplements are available for Figure 1:
745 **Figure 1 – Figure Supplement 1.** CjGrc3-activated CjLas1-catalytic ITS2
746 pre-rRNA cleavage.
747 **Figure 1 – Figure Supplement 2.** ScGrc3 has no ITS2 pre-rRNA cleavage
748 activity.
749 **Figure 1 – Figure Supplement 3.** Catalytic residues of Las1 HEPN domain
750 are necessary for ITS2 pre-rRNA cleavage.
751 **Figure 1 – Figure Supplement 4.** Characterization of the metal independence
752 of ITS2 pre-rRNA cleavage.
753
754 **Figure 2. Overall structure of ScLas1-Grc3 complex. (A)** Domain
755 organization of ScLas1 and ScGrc3. **(B)** Ribbon representations of
756 ScLas1-Grc3 complex. Color-coding used for Las1 and Grc3 is identical to that
757 used in Fig. 2a. **(C)** Surface representations of ScLas1-Grc3 complex.
758 Color-coding used for Las1 and Grc3 is identical to that used in Figure 2A.

759 The following figure supplement is available for Figure 2:
760 **Figure 2 – Figure Supplement 1. Single-particle cryo-EM analysis of the**
761 **ScLas1-Grc3 complex. (A)** Representative motion-corrected cryo-EM
762 micrograph. **(B)** Reference-free 2D class averages. **(C)** Workflow of the data
763 processing. **(D)** Euler angle distribution of the particle images. **(E)** Gold
764 standard FSC plot for the 3D reconstruction with full particle set, calculated in
765 cryoSPARC. **(F)** Resolution map for the final 3D reconstruction.
766
767 **Figure 3. Overall structure of CjLas1-Grc3 complex. (A)** Domain
768 organization of CjLas1 and CjGrc3. **(B)** Ribbon representations of CjLas1-Grc3

769 complex. Color-coding used for Las1 and Grc3 is identical to that used in Fig.
770 3a. **(C)** Surface representations of CjLas1-Grc3 complex. Color-coding used
771 for Las1 and Grc3 is identical to that used in Figure 3A.

772 The following figure supplements are available for Figure 3:
773 **Figure 3 – Figure Supplement 1. Single-particle cryo-EM analysis of the**
774 **CjLas1-Grc3 complex. (A)** Representative motion-corrected cryo-EM
775 micrograph. **(B)** Reference-free 2D class averages. **(C)** Workflow of the data
776 processing. **(D)** Euler angle distribution of the particle images. **(E)** Gold
777 standard FSC plot for the 3D reconstruction with full particle set, calculated in
778 cryoSPARC. **(F)** Resolution map for the final 3D reconstruction.
779 **Figure 3 – Figure Supplement 2. Comparison of cryo-EM and crystal**
780 **structures of Las1-Grc3 complexes. (A)** Superposition of the ScLas1-Grc3
781 complex crystal structure with the cryo-EM structure. Color-coding used for
782 ScLas1 and ScGrc3 in crystal structure is identical to that used in Fig. 2a.
783 ScLas1 and ScGrc3 in cryo-EM structure are colored in gray. **(B)**
784 Superposition of the CjLas1-Grc3 complex crystal structure with the cryo-EM
785 structure. Color-coding used for CjLas1 and CjGrc3 in crystal structure is
786 identical to that used in Fig. 3a. CjLas1 and CjGrc3 in cryo-EM structure are
787 colored in gray.
788 **Figure 3 – Figure Supplement 3. Sequence alignment of Las1 proteins.**
789 The ScLas1 protein was aligned with its respective homologs. Alignment was
790 performed using the MUSCLE program. The secondary structures of ScLas1
791 and CjLas1 are shown above and below the sequences, respectively.
792 Conserved residues are highlighted in yellow, and invariant residues are
793 highlighted in red. Catalytic residues in Las1 HEPN domain are marked in
794 violet triangles. The figure was prepared using ESPript3.
795
796 **Figure 4. The CC domain contributes to ITS2 RNA binding and cleavage.**

797 **(A)** Structural comparison between ScLas1-Grc3 complex and CjLas1-Grc3
798 complex. Color-coding used for ScLas1 and ScGrc3 is identical to that used in
799 Fig. 2a. The CC domain of CjLas1 is colored in salmon, other domains of
800 CjLas1 and all domains of CjGrc3 are colored in gray. **(B)** Structures of CjLas1
801 CC domain (in salmon) and ScLas1 CC domain (in lightmagenta). **(C)** *In vitro*
802 RNA cleavage assay using indicated truncations of ScLas1. **(D)**
803 Electrophoretic mobility shift assay using indicated truncations of ScLas1.
804
805 **Figure 5. ScGrc3 GCT mediates the ITS2 cleavage activity of ScLas1. (A)**
806 ScGrc3 GCT binds at an active channel of ScLas1 HEPN dimer. Two HEPN
807 domains of Las1 are colored in pink and violet, respectively. GCTs of Grc3 are
808 colored in teal. The catalytic site is highlighted in yellow. HEPN domains are
809 shown as surfaces, while GCTs are shown as sticks. **(B)** Detailed interactions
810 between ScGrc3 GCT and ScLas1 HEPN domain. **(C)** Sequence alignments
811 of Grc3 GCTs. Identical residues are highlighted in red. Basically constant
812 residuals are shaded in blue. Conserved residues are shaded in orange. **(D)** *In*
813 *vitro* enzymatic assay of mutations of ScGrc3 residues Glu614, His615 and
814 Trp617. **(E)** GST pull-down experiment assaying the ability of ScGrc3 mutants
815 to interact with ScLas1. **(F)** *In vitro* enzymatic assay of alanine mutations of
816 ScGrc3 C-terminal residues.

817 The following figure supplement is available for Figure 5:
818 **Figure 5 – Figure Supplement 1.** *In vitro* enzymatic assay of alanine
819 mutations of conserved CjGrc3 residues Trp618, Arg601, Arg606 and Arg607.
820
821 **Figure 6. Las1 LCT drives Las1-Grc3 cross talk. (A)** ScLas1 LCT binds to
822 the CTD domain of ScGrc3. ScGrc3 is shown as surface, ScLas1 LCT is
823 shown as stick. **(B)** Detailed interactions between C-terminal residues of
824 ScLas1 LCT and ScGrc3 CTD domain. **(C)** Detailed interactions between

825 N-terminal residues of ScLas1 LCT and ScGrc3 CTD domain.

826 The following figure supplements are available for Figure 6:

827 **Figure 6 – Figure Supplement 1.** Denaturing gel showing the ITS2 pre-RNA
828 cleavage by mutation or deletion of the interacting residues of ScLas1 LCT.

829 **Figure 6 – Figure Supplement 2.** GST pull-down experiment assaying the
830 Grc3 binding ability by mutation or deletion of the interacting residues of
831 ScLas1 LCT.

832

833 **Figure 7. Activation mechanism of Las1 by Grc3. (A)** Crystal structure of
834 CjLas1 HEPN domain. **(B)** The HEPN3 molecule (in slate) and its
835 symmetry-related molecule (in bluewhite) in Las1 HEPN domain structure. **(C)**
836 The HEPN1 (in pink) and HEPN2 (in violet) molecules in Las1 HEPN domain
837 structure. **(D)** Structural comparison of HEPN dimers between CjLas1-Grc3
838 complex (Las1A HEPN in pink, Las1B HEPN in violet) and CjLas1 HEPN
839 domain (in gray). Inset: a magnified view of the comparison of the catalytic site
840 in the two structures.

841 The following figure supplements are available for Figure 7:

842 **Figure 7 – Figure Supplement 1.** Structural superposition of HEPN3 (in slate)
843 and its symmetry-related molecule (in bluewhite) with the HEPN1(in
844 pink)-HEPN2 (in violet) dimer.

845 **Figure 7 – Figure Supplement 2.** Structural comparison of HEPN dimers
846 between ScLas1-Grc3 complex (Las1A HEPN in pink, Las1B HEPN in violet)
847 and CjLas1 HEPN domain (in gray). Inset: a magnified view of the comparison
848 of the catalytic site in the two structures.

849

850 **Figure 8. Model for Grc3-mediated Las1-catalyzed ITS2 pre-rRNA**
851 **processing.** Prior to assembly with Grc3, Las1 shows weak processing
852 activity for ITS2 precursor RNA. When combined with Grc3 to form a tetramer

853 complex, Las1 shows high processing activity for ITS2 precursor RNA. Las1
854 specifically cleaves ITS2 at C2 and C2′ sites to generate 5′-OH terminus
855 products. The 5′-OH terminus products are further phosphorylated by Grc3
856 when in the presence of ATP.

857 The following figure supplement is available for Figure 8:

858 **Figure 8 – Figure Supplement 1. Comparison of Las1-Grc3, Ire1 and**
859 **RNase L.** Comparison of structural assembly, activation and substrate
860 recognition mechanisms of Las1-Grc3, Ire1 and RNase L. Two HEPN domains
861 in Las1, Ire1 and RNase L are colored in pink and violet, respectively. Two
862 PNK domains in Grc3, two Kinase domains in Ire1, and two Preudo-Kinase
863 domains in RNase L, are colored in cyan and greencyan, respectively. The
864 catalytic site is highlighted with a yellow box.
865

866 **Table 1. Crystallographic data collection and refinement statistics.**

	ScLas1-Grc3	CjLas1-Grc3	CjLas1
Data collection*			
Space group	*C*2	$C222_1$	$P2_12_12_1$
Cell dimensions			
a, *b*, *c* (Å)	233.6, 116.1, 159.3	152.6, 240.0, 237.0	51.5, 59.0, 158.7
α, β, γ (°)	90.0, 96.4, 90.0	90.0, 90.0, 90.0	90.0, 90.0, 90.0
Resolution (Å)	50.00-3.50 (3.56-3.50)	50.00-3.23 (3.29-3.23)	50.00-1.80 (1.83-1.80)
R_{merge}	0.298 (0.980)	0.344 (0.958)	0.103 (0.929)
$I/\sigma I$	4.8 (1.1)	4.3 (1.6)	22.0 (2.5)
Completeness (%)	98.8 (96.5)	99.9 (99.9)	97.7 (95.8)
Redundancy	4.5 (3.5)	7.5 (6.4)	10.1 (9.5)
Refinement			
Resolution (Å)	3.69	3.39	1.80
No. reflections	36,773	41,321	44,296
R_{work} / R_{free}	0.2798/0.3151	0.3041/0.3281	0.2120/0.2334
No. atoms			
protein	22,873	18,763	3,657
Water	180	386	212
B-factors (Å^2)			
Protein	95.5	125.6	23.3
Water	33.2	55.9	28.5
R.m.s. deviations			
Bond length (Å)	0.008	0.011	0.015
Bond angles (°)	1.516	1.785	1.500
Ramachandran plot			
Favored region	94.96	95.72	97.98
Allowed region	4.86	4.28	2.02
Outlier region	0.18	0.00	0.00

867 * Highest resolution shell is shown in parentheses.

868

869 **Table 2. Cryo-EM data collection and processing.**

	ScLas1-Grc3	CjLas1-Grc3
Data collection and processing		
Microscope	Titan Krios	Titan Krios
Voltage (kV)	300	300
Camera	Gatan K3	Gatan K3
Magnification	105,000x	105,000x
Pixel size (Å)	0.82	0.82
Total exposure (e-/Å^2)	50	50
Exposure time (s)	3	3
Number of frames per exposure	30	30
Energy filter slit width (keV)	20	20
Data collection software	EPU	EPU
Defocus range (μm)	-1.3 - -2.7	-1.2 - -3
Number of micrographs	2,520	8,616
Number of initial particles	525,213	2,215,555
Symmetry	C2	C2
Number of final particles	264,341	523,843
Resolution (0.143 gold standard FSC, Å)	3.07	3.39
Local resolution range (Å)	2.8-4.8	2.8-4.8

870

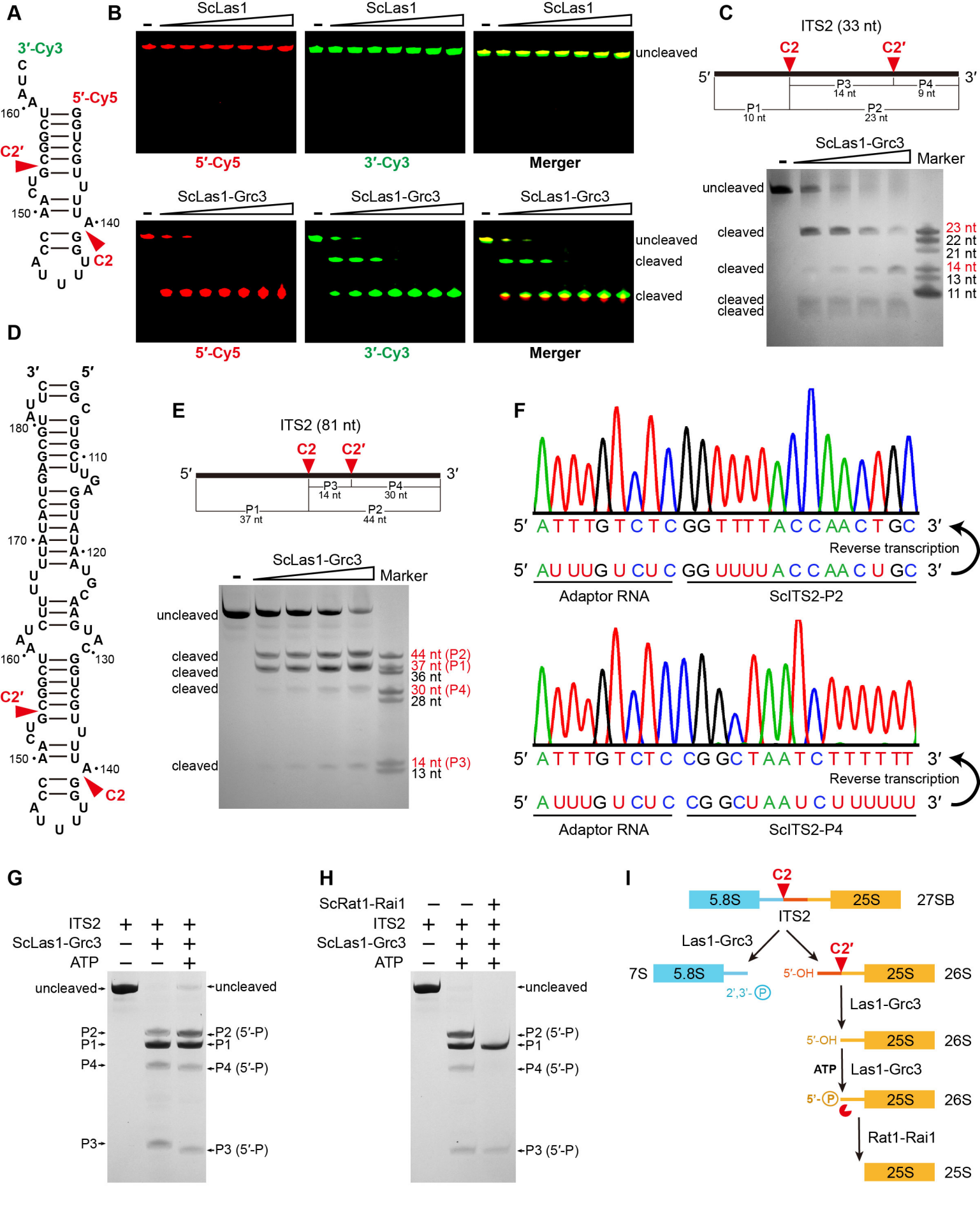
A
3′-Cy3
5′-Cy5
C2′
C2
B
ScLas1
ScLas1-Grc3
uncleaved
cleaved
5′-Cy5
3′-Cy3
Merger
C
ITS2 (33 nt)
C2
C2′
5′
3′
P1
10 nt
P2
23 nt
P3
14 nt
P4
9 nt
ScLas1-Grc3
Marker
uncleaved
cleaved
23 nt
22 nt
21 nt
14 nt
13 nt
11 nt
D
E
ITS2 (81 nt)
P1
37 nt
P2
44 nt
P3
14 nt
P4
30 nt
44 nt (P2)
37 nt (P1)
36 nt
30 nt (P4)
28 nt
14 nt (P3)
13 nt
F
Reverse transcription
Adaptor RNA
ScITS2-P2
ScITS2-P4
G
ITS2
ScLas1-Grc3
ATP
uncleaved
P2
P1
P4
P3
P2 (5′-P)
P4 (5′-P)
P3 (5′-P)
H
ScRat1-Rai1
I
5.8S
25S
27SB
ITS2
Las1-Grc3
7S
26S
5′-OH
2′,3′-P
ATP
Rat1-Rai1

Figure 1

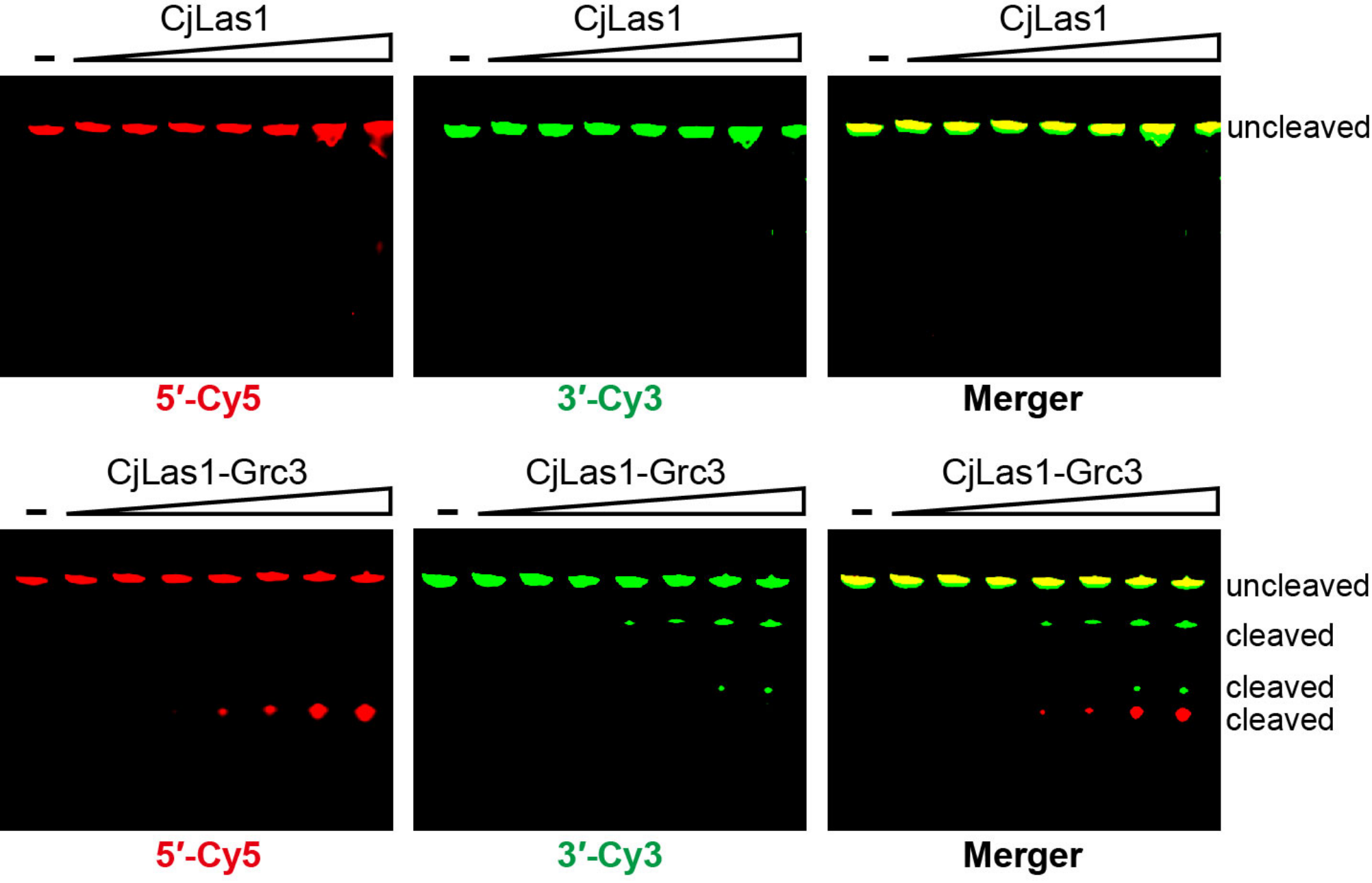

Figure 1—figure supplement 1

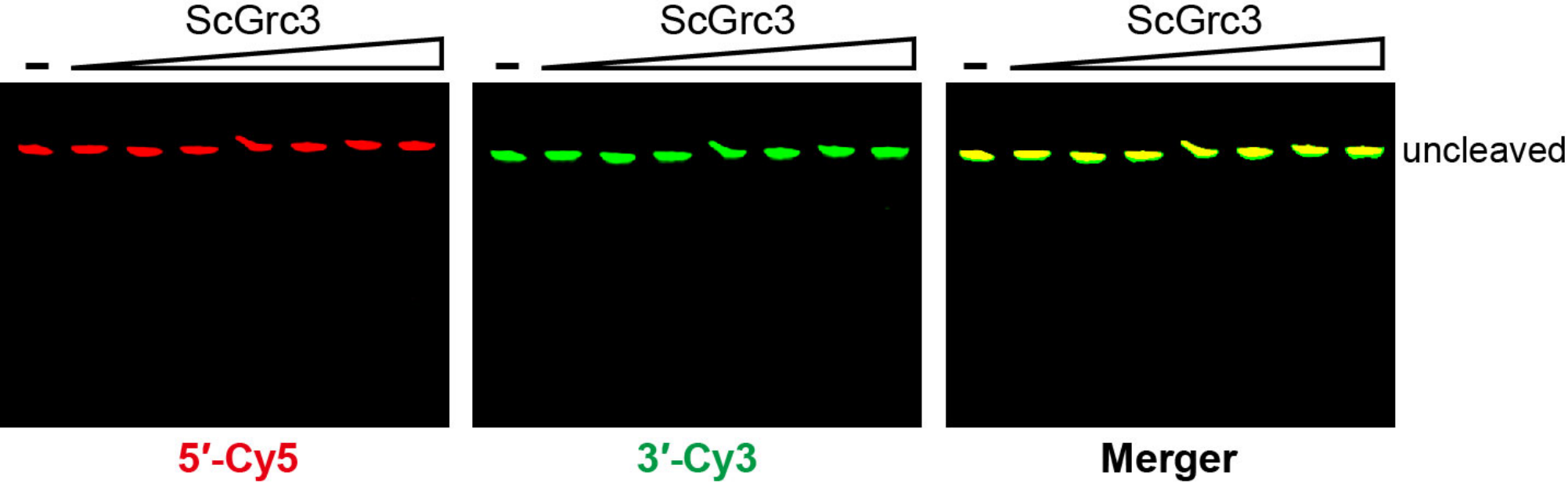

Figure 1—figure supplement 2

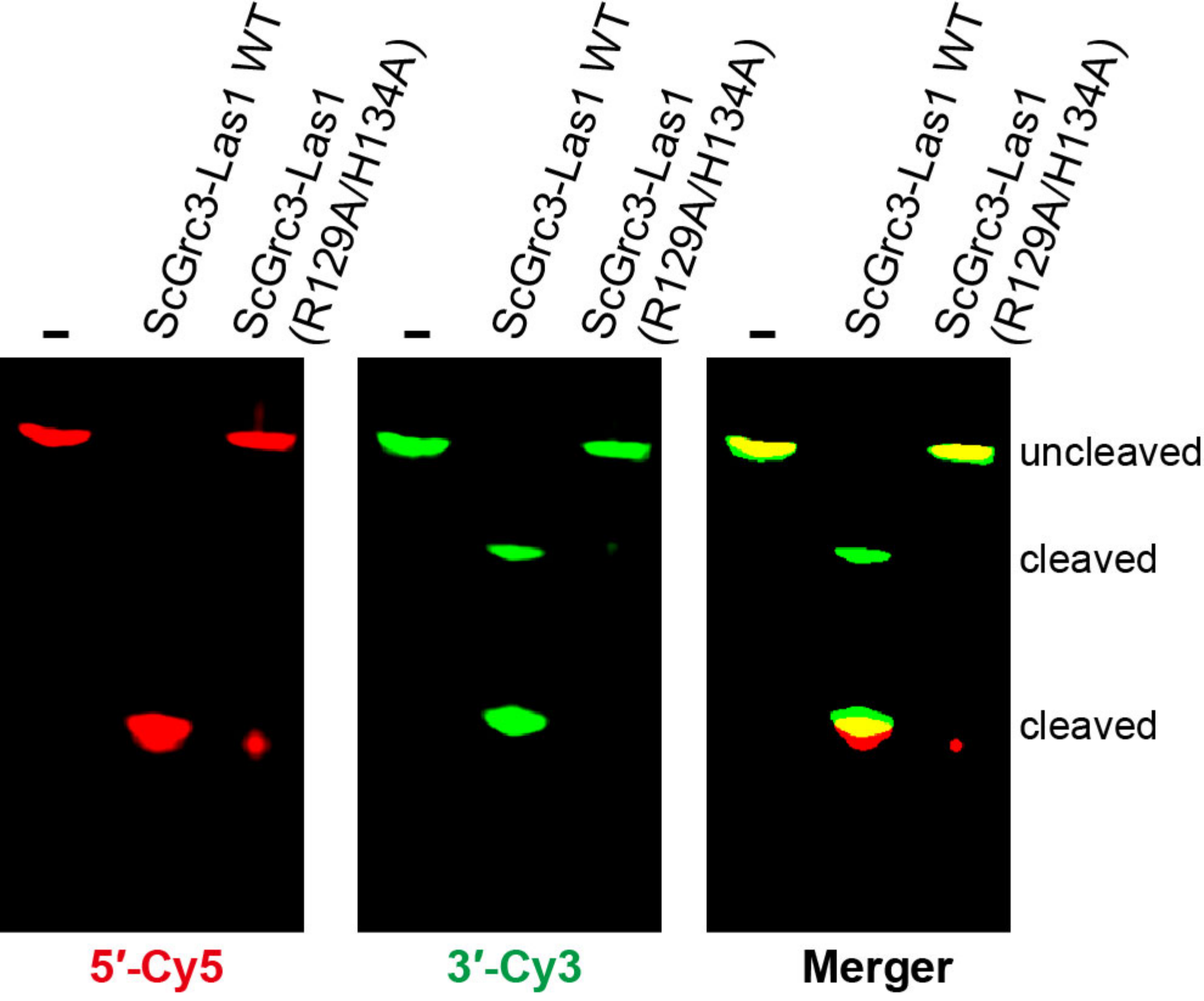

Figure 1—figure supplement 3

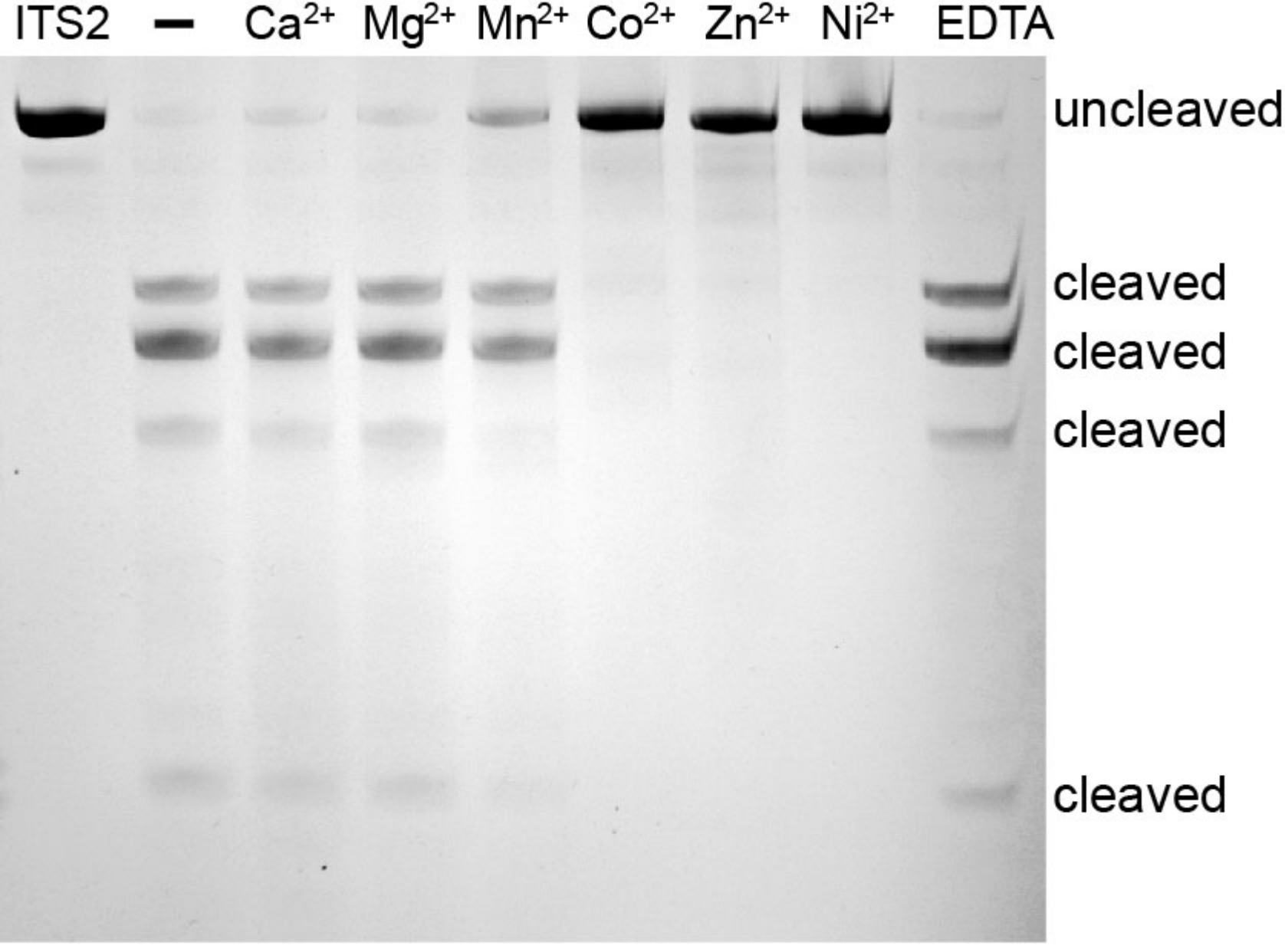

Figure 1—figure supplement 4

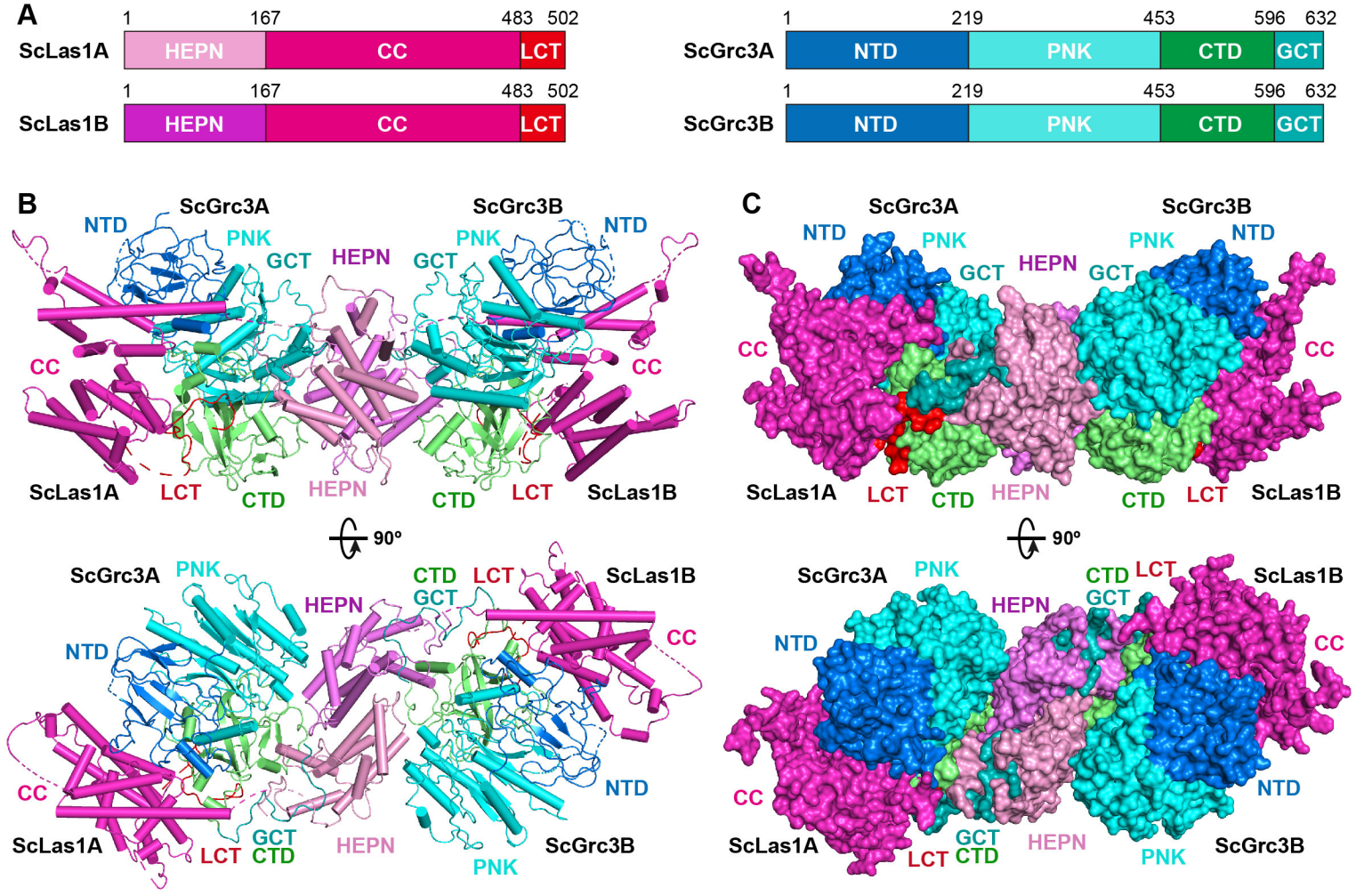
A
ScLas1A
1
167
483
502
HEPN
CC
LCT
ScLas1B
1
167
483
502
HEPN
CC
LCT
ScGrc3A
1
219
453
596
632
NTD
PNK
CTD
GCT
ScGrc3B
1
219
453
596
632
NTD
PNK
CTD
GCT
B
ScGrc3A
ScGrc3B
NTD
PNK
GCT
HEPN
CC
ScLas1A
LCT
CTD
ScLas1B
90°
C
ScGrc3A
ScGrc3B
NTD
PNK
GCT
HEPN
CC
ScLas1A
LCT
CTD
ScLas1B
90°

Figure 2

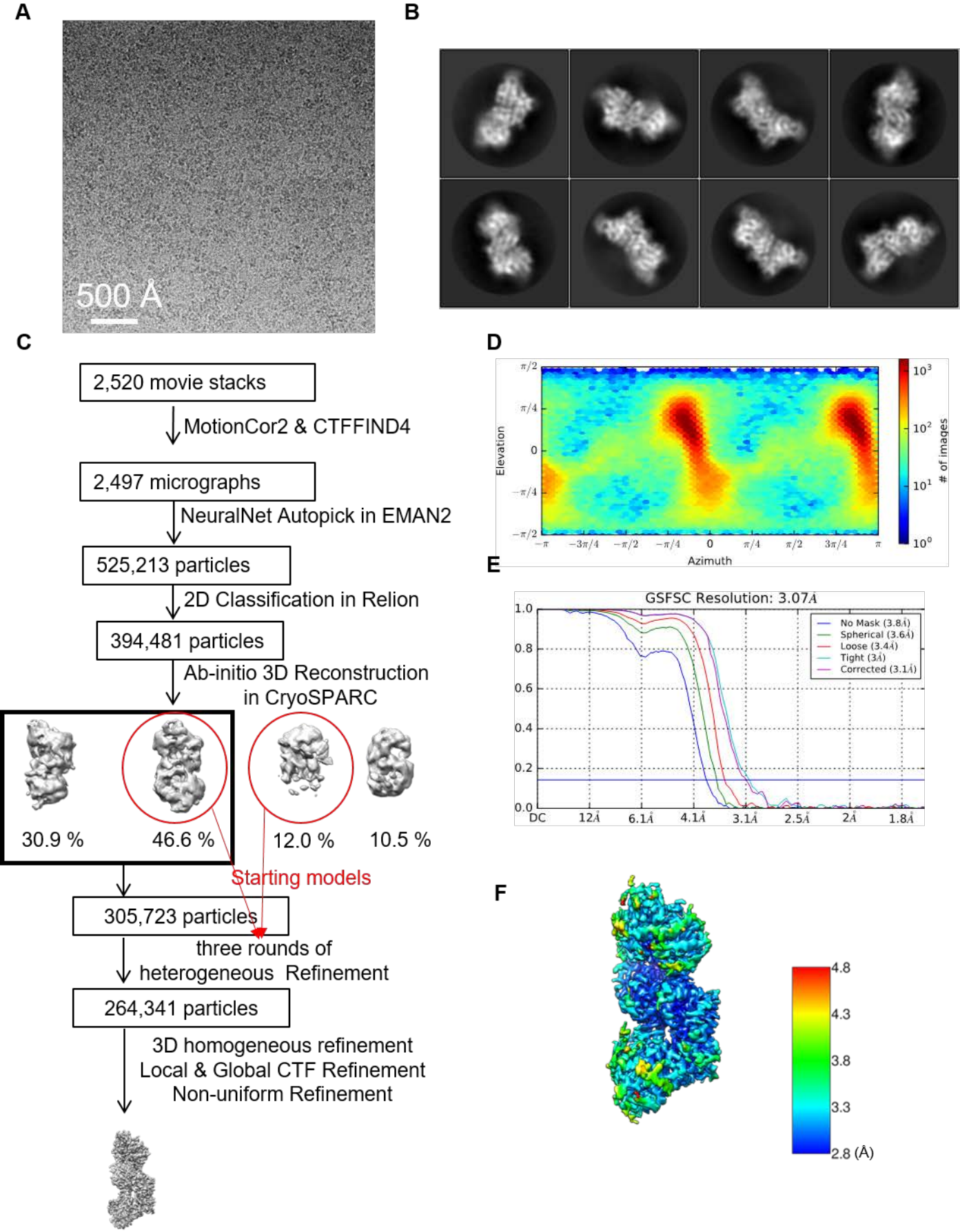

Figure 2-figure supplement 1

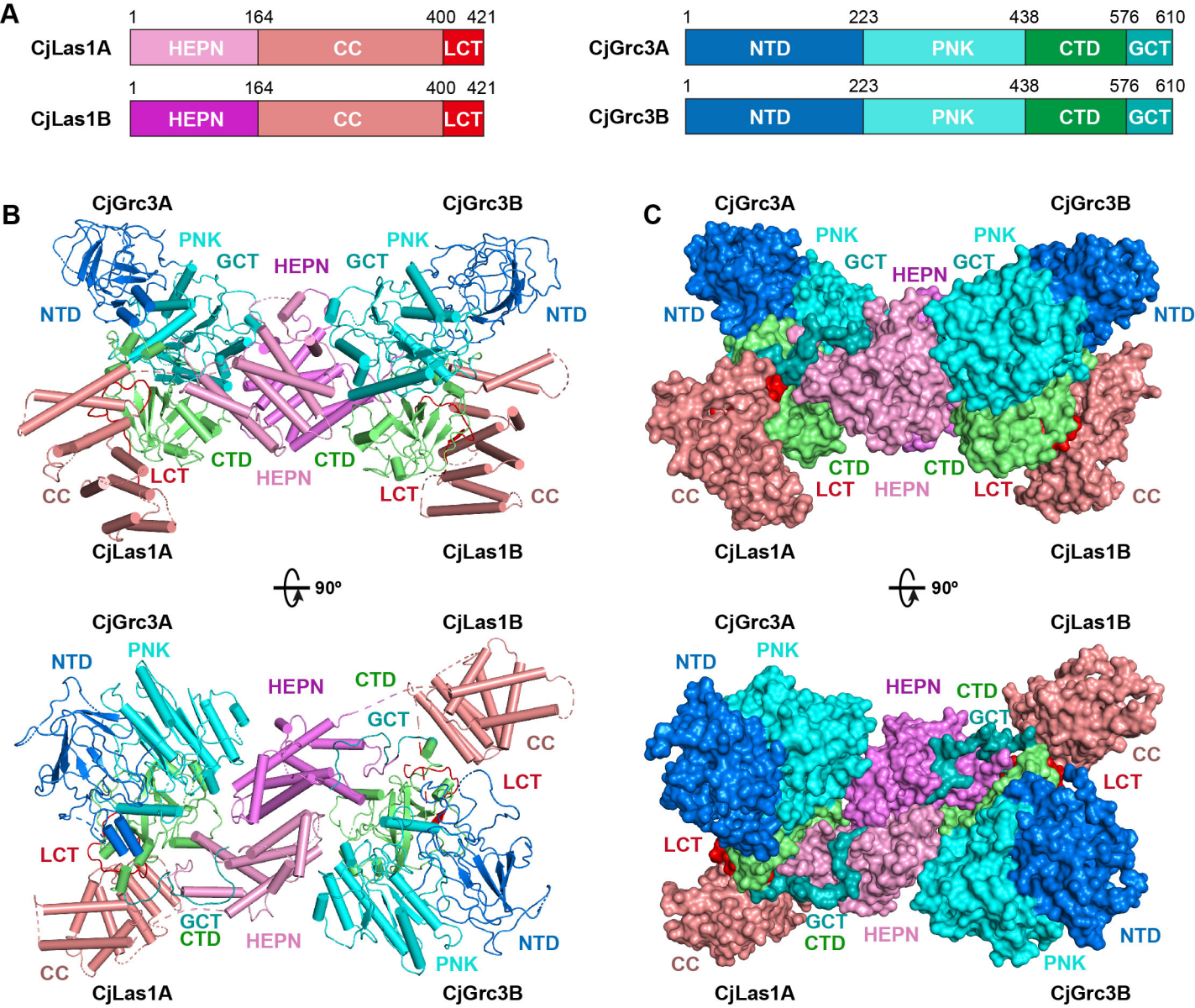
A
CjLas1A
1
164
400
421
HEPN
CC
LCT
CjLas1B
1
164
400
421
HEPN
CC
LCT
CjGrc3A
1
223
438
576
610
NTD
PNK
CTD
GCT
CjGrc3B
1
223
438
576
610
NTD
PNK
CTD
GCT
B
CjGrc3A
CjGrc3B
PNK
GCT
HEPN
GCT
PNK
NTD
NTD
CTD
CTD
LCT
HEPN
LCT
CC
CC
CjLas1A
CjLas1B
90°
CjGrc3A
CjLas1B
NTD
PNK
HEPN
CTD
GCT
CC
LCT
LCT
GCT
CTD
HEPN
NTD
CC
PNK
CjLas1A
CjGrc3B
C
CjGrc3A
CjGrc3B
PNK
GCT
HEPN
GCT
PNK
NTD
NTD
CTD
CTD
CC
LCT
HEPN
LCT
CC
CjLas1A
CjLas1B
90°
CjGrc3A
CjLas1B
NTD
PNK
HEPN
CTD
GCT
CC
LCT
LCT
GCT
CTD
HEPN
NTD
CC
PNK
CjLas1A
CjGrc3B

Figure 3

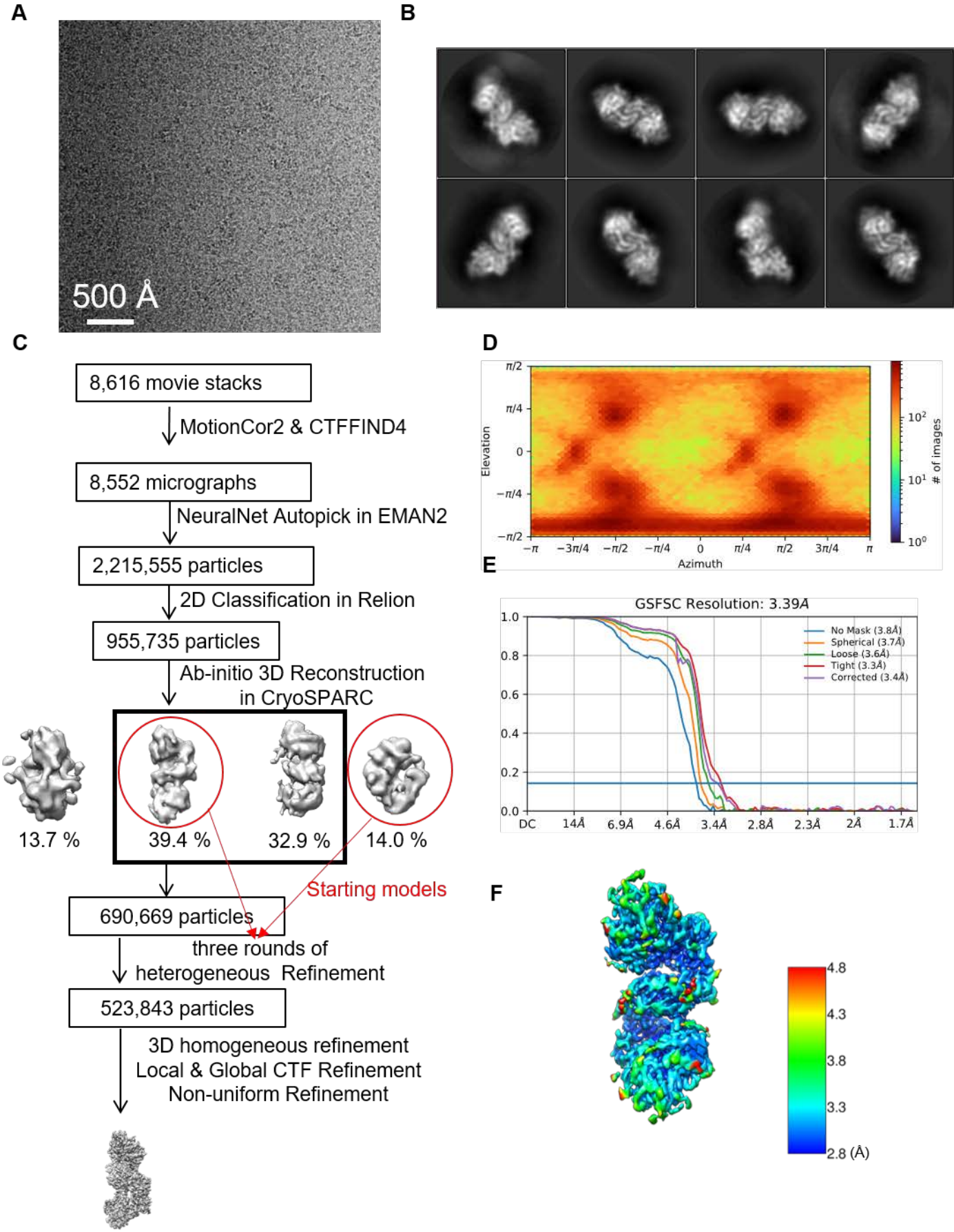

Figure 3—figure supplement 1

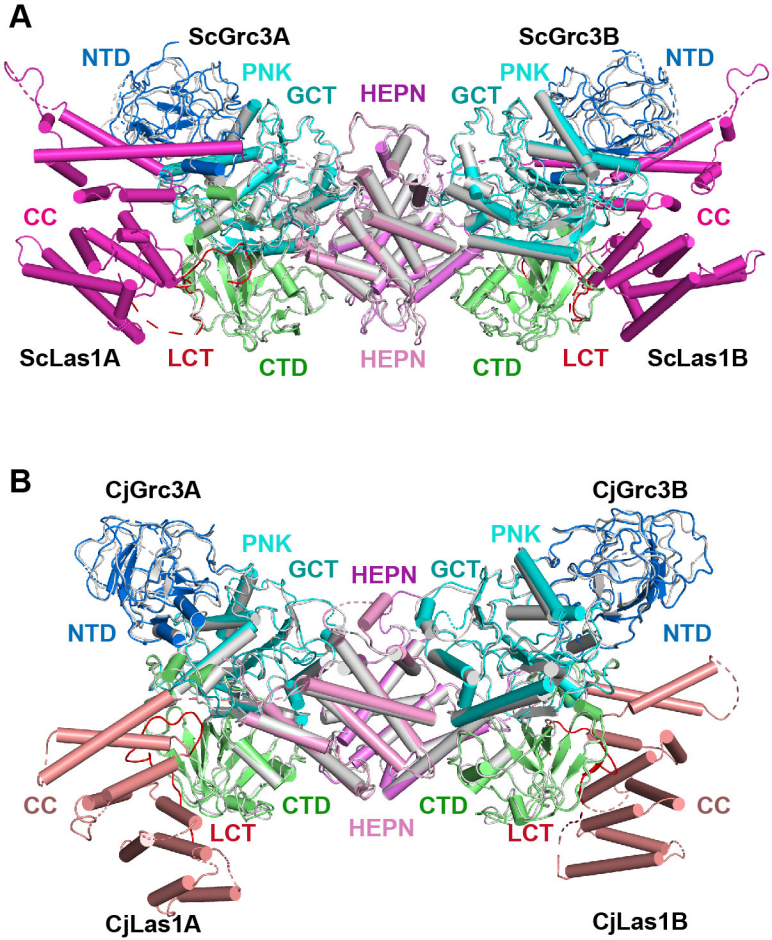

Figure 3—figure supplement 2

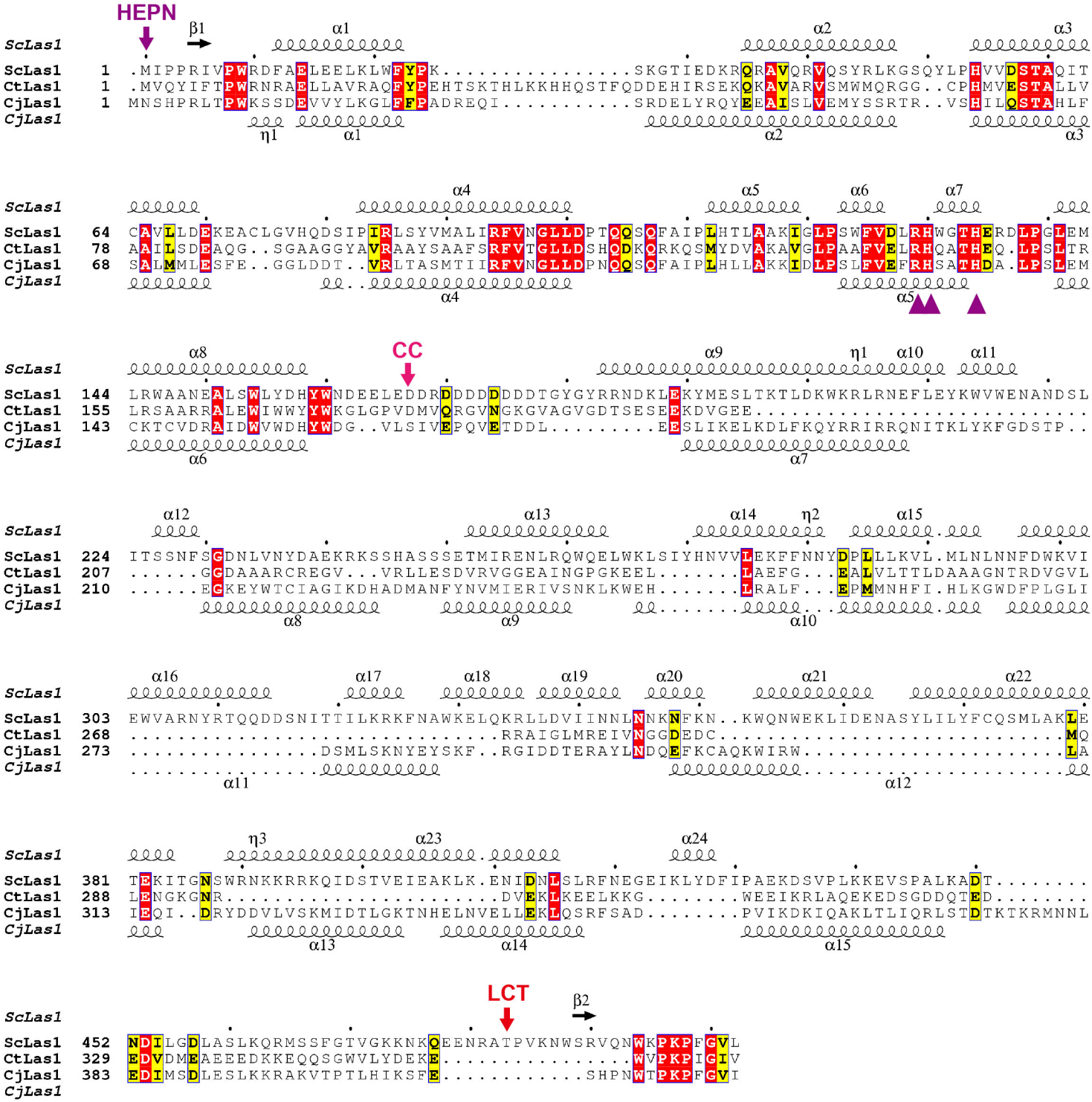

Figure 3—figure supplement 3

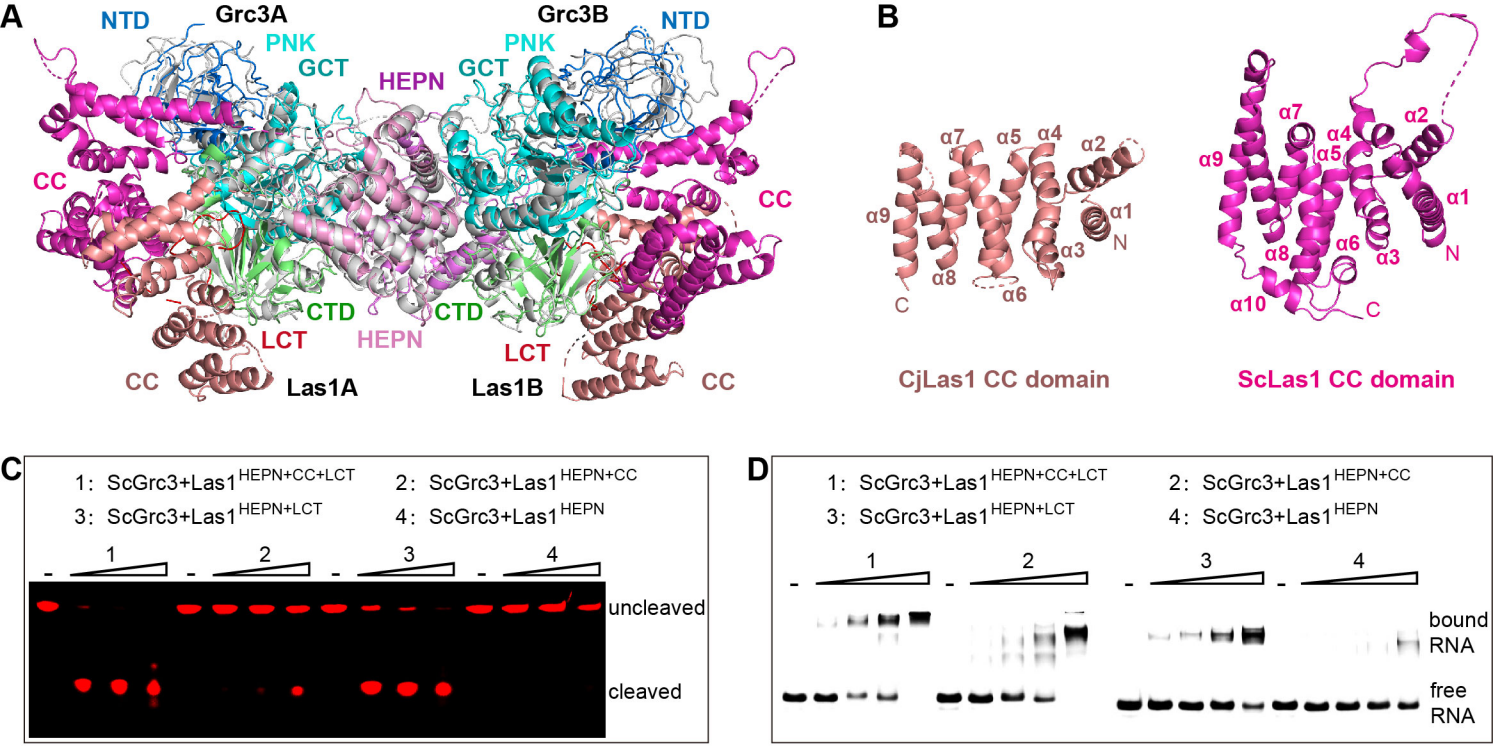
A
NTD
Grc3A
PNK
GCT
HEPN
Grc3B
PNK
GCT
NTD
CC
CC
CTD
CTD
LCT
HEPN
LCT
CC
Las1A
Las1B
CC
B
α7
α5
α4
α2
α9
α1
N
α3
α8
α6
C
CjLas1 CC domain
α7
α2
α4
α5
α9
α1
α8
α6
α3
N
α10
C
ScLas1 CC domain
C
1: ScGrc3+Las1HEPN+CC+LCT
2: ScGrc3+Las1HEPN+CC
3: ScGrc3+Las1HEPN+LCT
4: ScGrc3+Las1HEPN
1
2
3
4
uncleaved
cleaved
D
1: ScGrc3+Las1HEPN+CC+LCT
2: ScGrc3+Las1HEPN+CC
3: ScGrc3+Las1HEPN+LCT
4: ScGrc3+Las1HEPN
1
2
3
4
bound RNA
free RNA

Figure 4

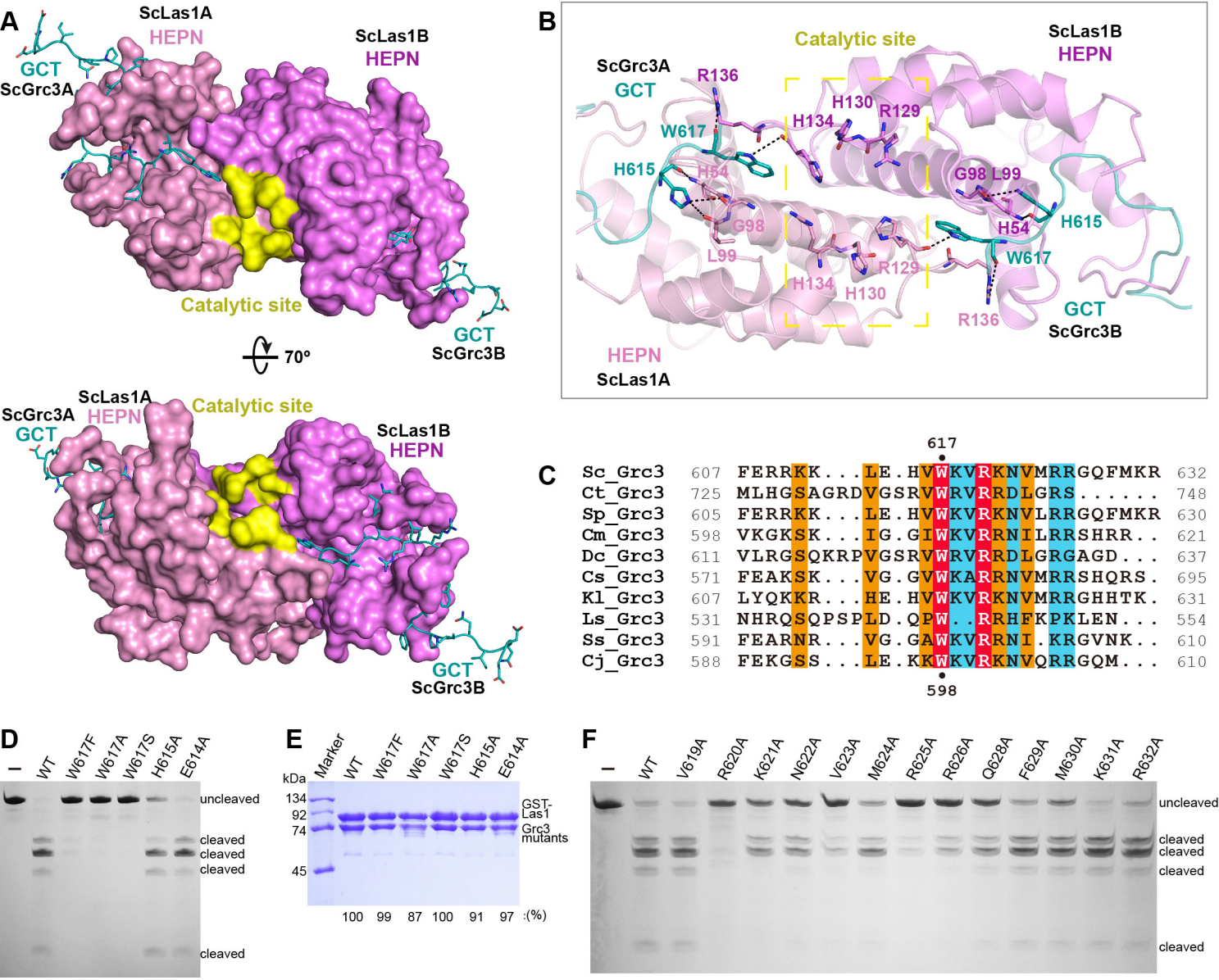
A
ScLas1A
HEPN
GCT
ScGrc3A
ScLas1B
HEPN
Catalytic site
GCT
ScGrc3B
70°
ScLas1A
HEPN
ScGrc3A
GCT
Catalytic site
ScLas1B
HEPN
GCT
ScGrc3B
B
Catalytic site
ScLas1B
HEPN
ScGrc3A
GCT
R136
H130
R129
H134
W617
H615
H54
G98
L99
G98 L99
H615
H54
W617
L99
R129
H134
H130
R136
GCT
ScGrc3B
HEPN
ScLas1A
C
617
Sc_Grc3 607 FERRKK...LE.HVWKVRKNVMRRGQFMKR 632
Ct_Grc3 725 MLHGSAGRDVGSRVWRVRRDLGRS..... 748
Sp_Grc3 605 FERRKK...LE.HVWKVRKNVLRRGQFMKR 630
Cm_Grc3 598 VKGKSK...IG.GIWKVRRNILRRSHRR.. 621
Dc_Grc3 611 VLRGSQKRPVGSRVWRVRRDLGRGAGD... 637
Cs_Grc3 571 FEAKSK...VG.GVWKARRNVMRRSHQRS. 695
Kl_Grc3 607 LYQKKR...HE.HVWKVRKNVMRRGHHTK. 631
Ls_Grc3 531 NHRQSQPSPLD.QPW..RRHFKPKLEN... 554
Ss_Grc3 591 FEARNR...VG.GAWKVRRNI.KRGVNK.. 610
Cj_Grc3 588 FEKGSS...LE.KKWKVRKNVQRRGQM... 610
598
D
–
WT
W617F
W617A
W617S
H615A
E614A
uncleaved
cleaved
cleaved
cleaved
cleaved
E
Marker
WT
W617F
W617A
W617S
H615A
E614A
kDa
134
92
74
45
GST-Las1
Grc3 mutants
100 99 87 100 91 97 :(%)
F
–
WT
V619A
R620A
K621A
N622A
V623A
M624A
R625A
R626A
Q628A
F629A
M630A
K631A
R632A
uncleaved
cleaved
cleaved
cleaved
cleaved

Figure 5

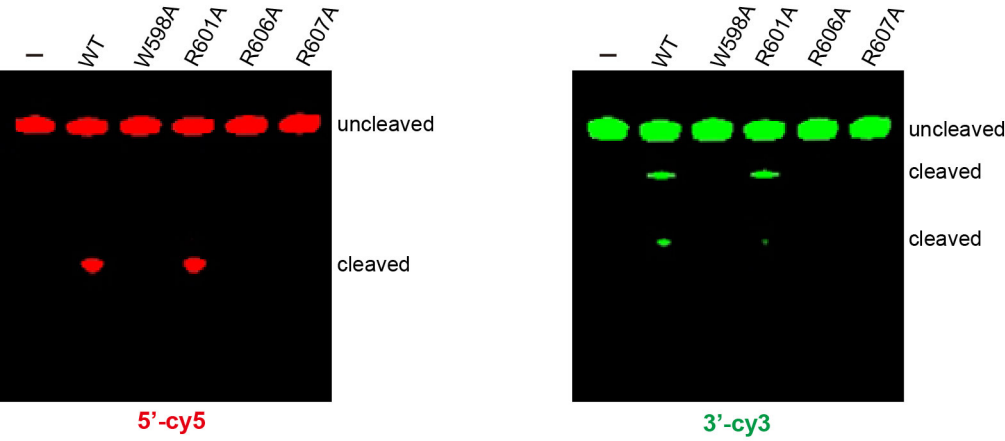

Figure 5—figure supplement 1

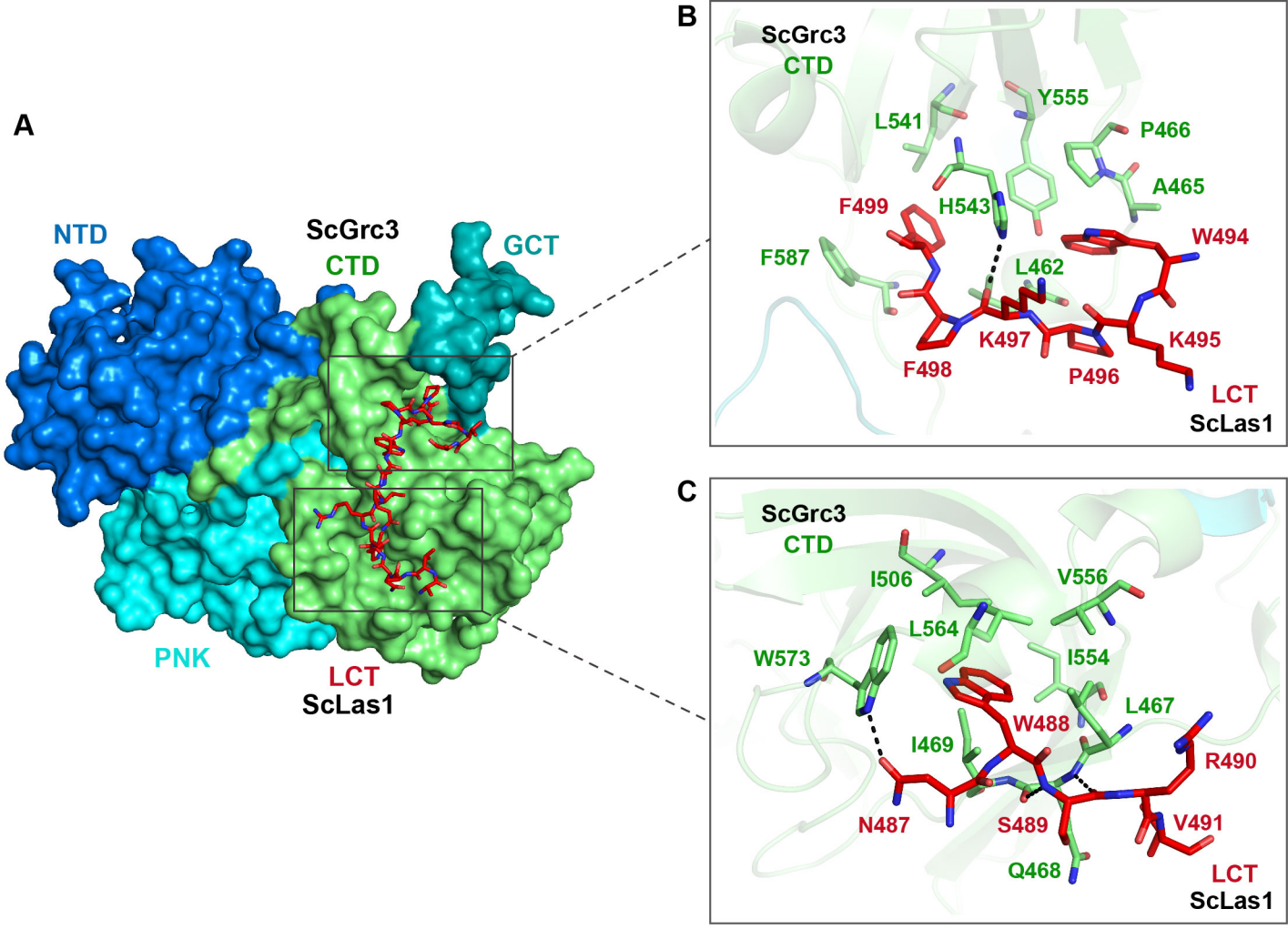
A
NTD
ScGrc3
CTD
GCT
PNK
LCT
ScLas1
B
ScGrc3
CTD
L541
Y555
P466
A465
F499
H543
W494
F587
L462
K497
K495
F498
P496
LCT
ScLas1
C
ScGrc3
CTD
I506
V556
L564
W573
I554
L467
W488
I469
R490
N487
S489
V491
Q468
LCT
ScLas1

Figure 6

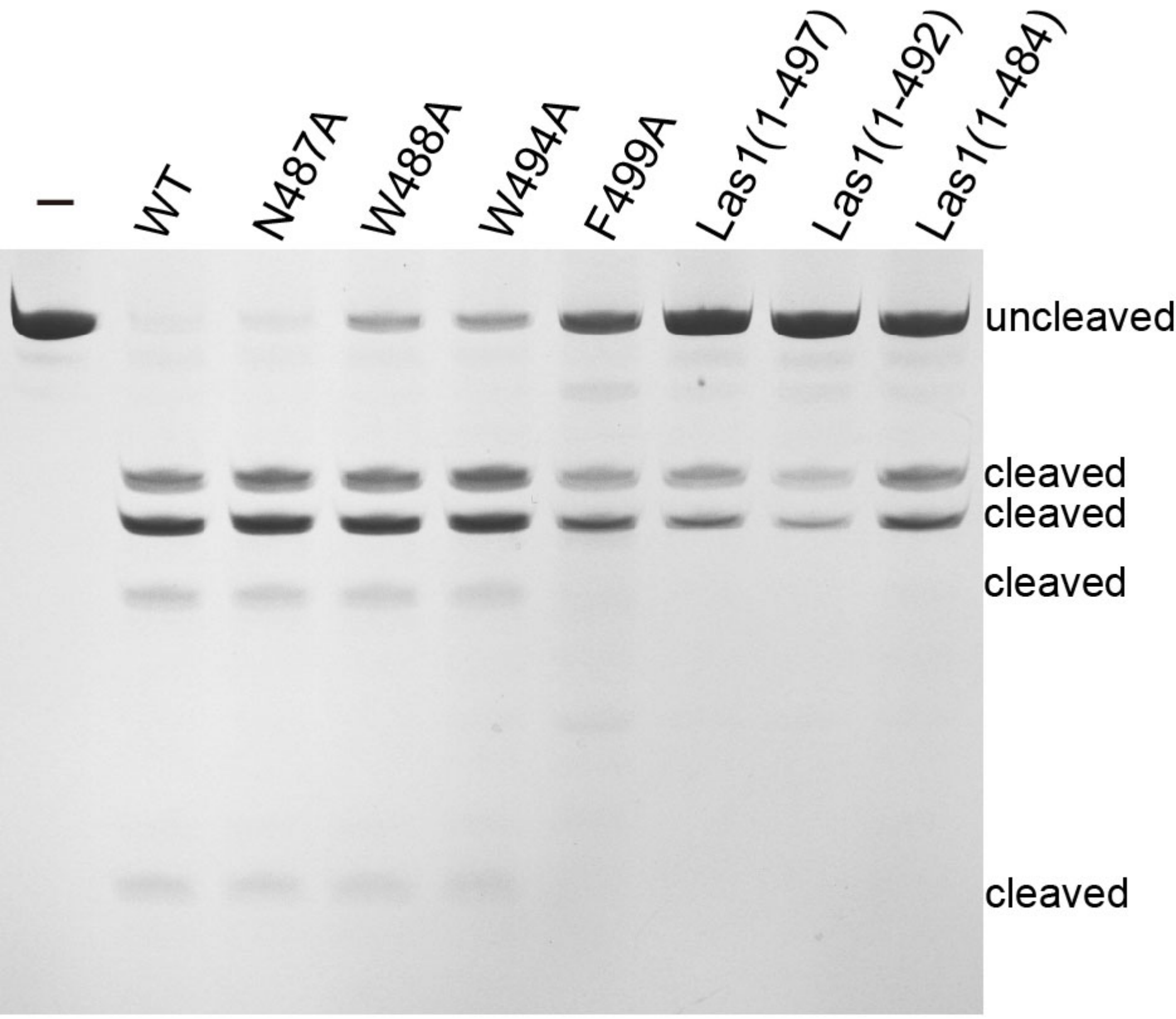

Figure 6—figure supplement 1

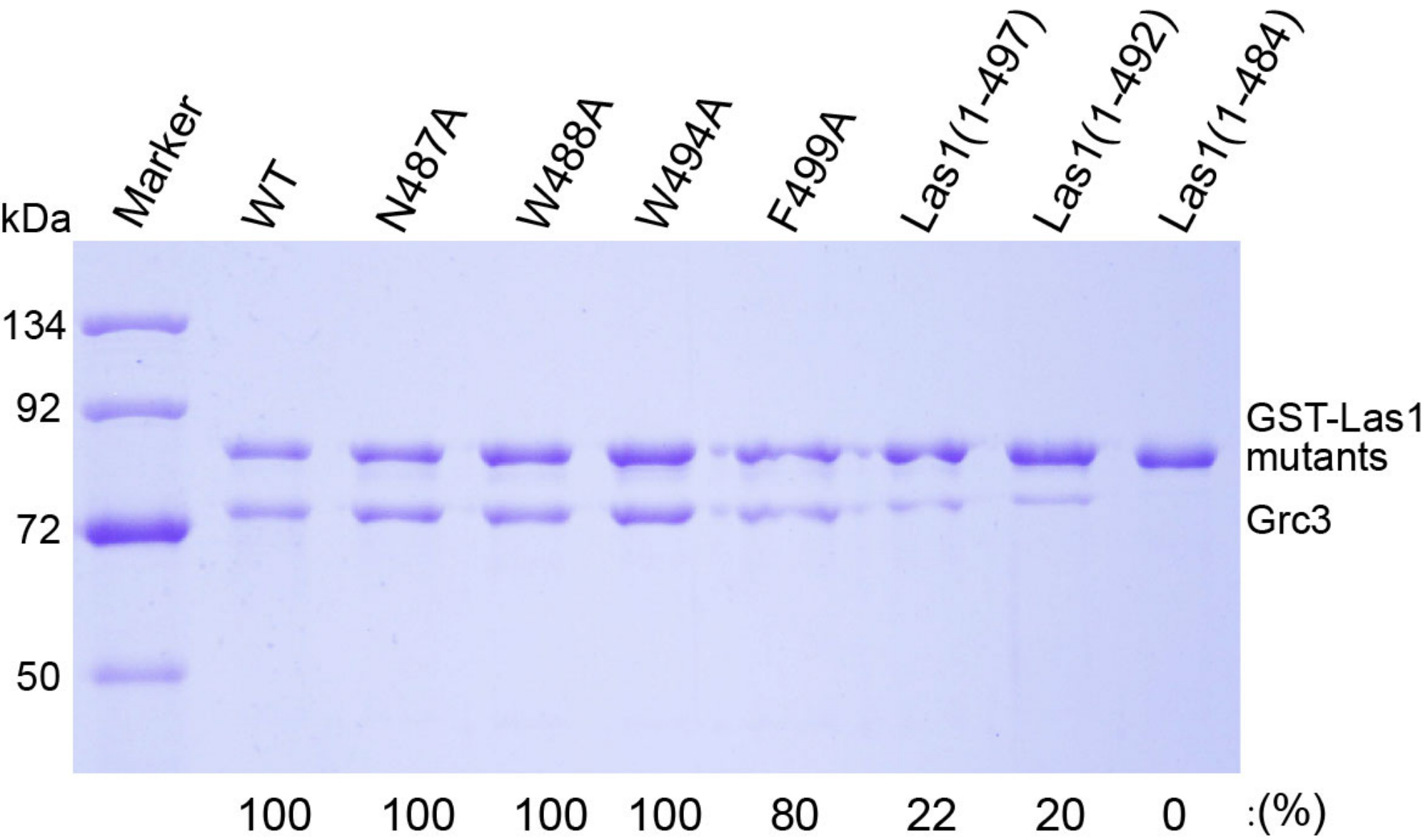

Figure 6—figure supplement 2

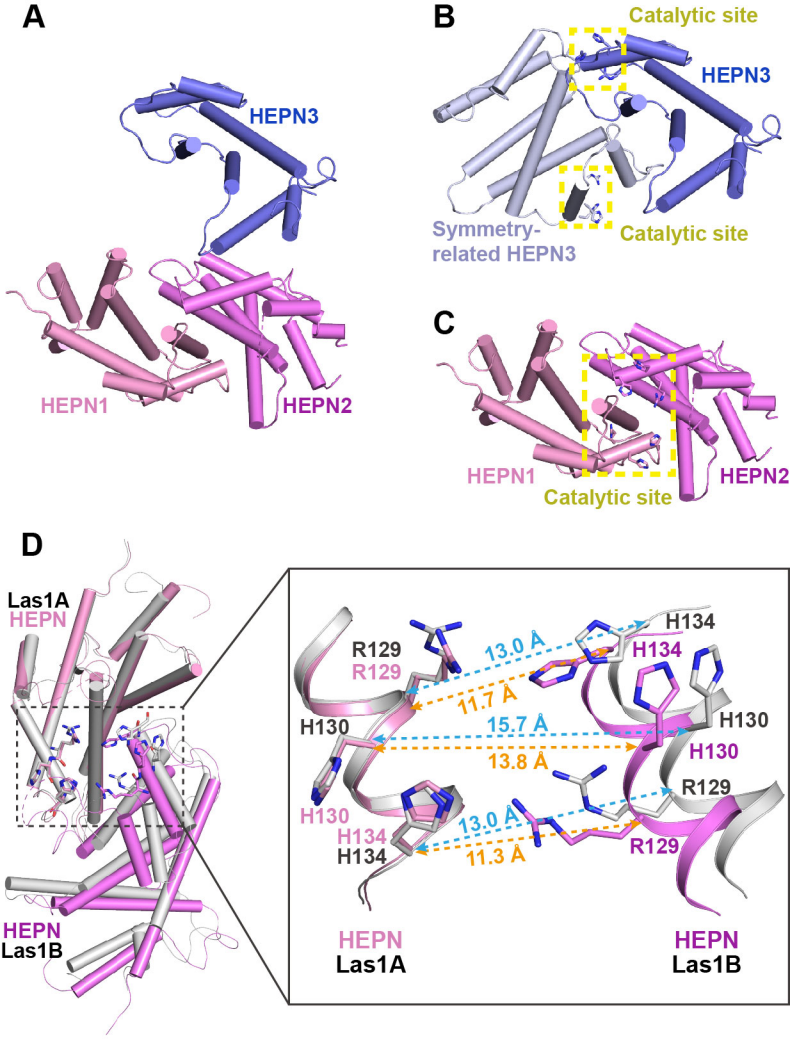
A
HEPN3
HEPN1
HEPN2
B
Catalytic site
HEPN3
Symmetry-
related HEPN3
Catalytic site
C
HEPN1
HEPN2
Catalytic site
D
Las1A
HEPN
HEPN
Las1B
R129
R129
13.0 Å
H134
H134
11.7 Å
H130
15.7 Å
H130
13.8 Å
H130
R129
H130
13.0 Å
H134
H134
11.3 Å
R129
HEPN
Las1A
HEPN
Las1B

Figure 7

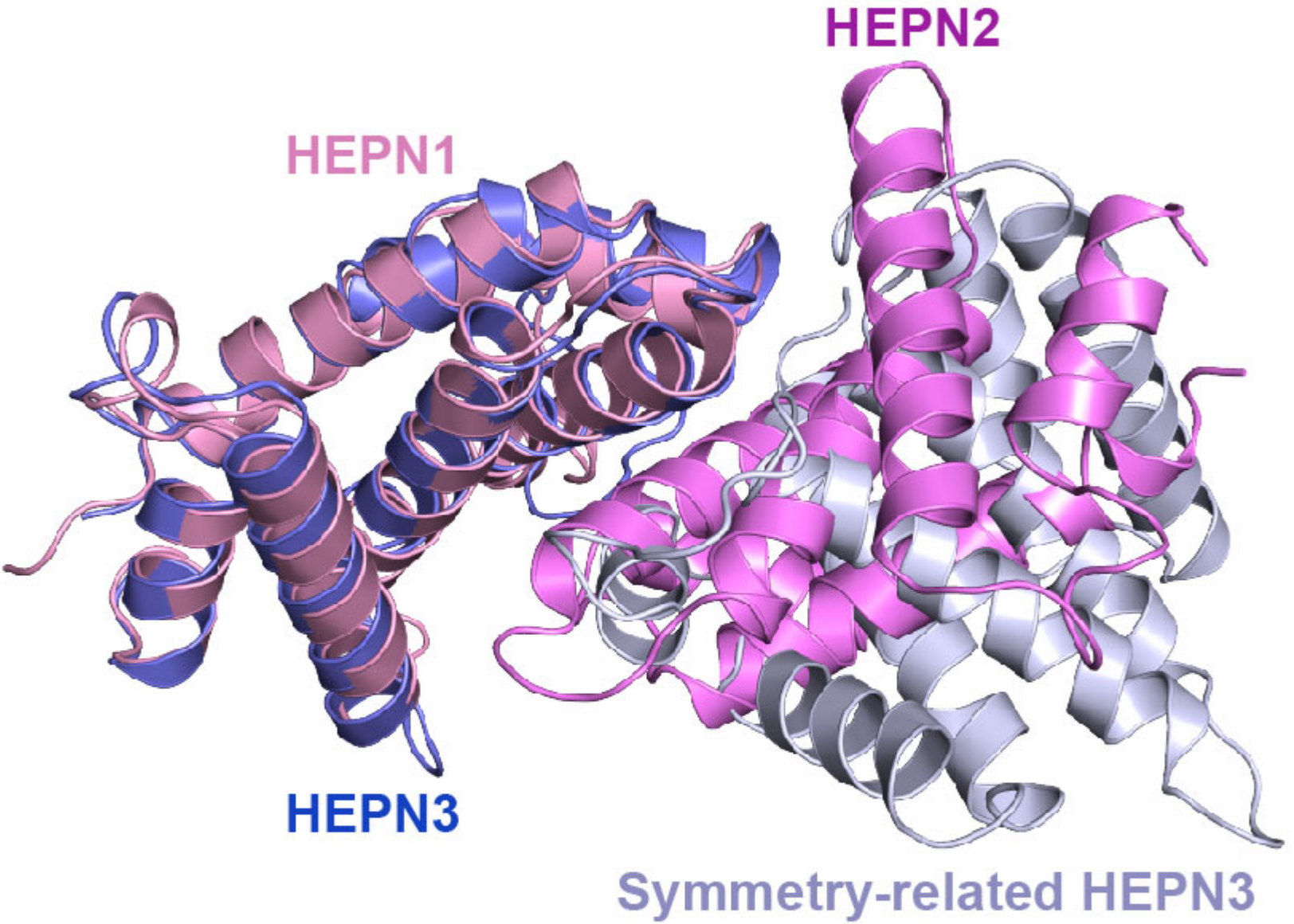

Figure 7—figure supplement 1

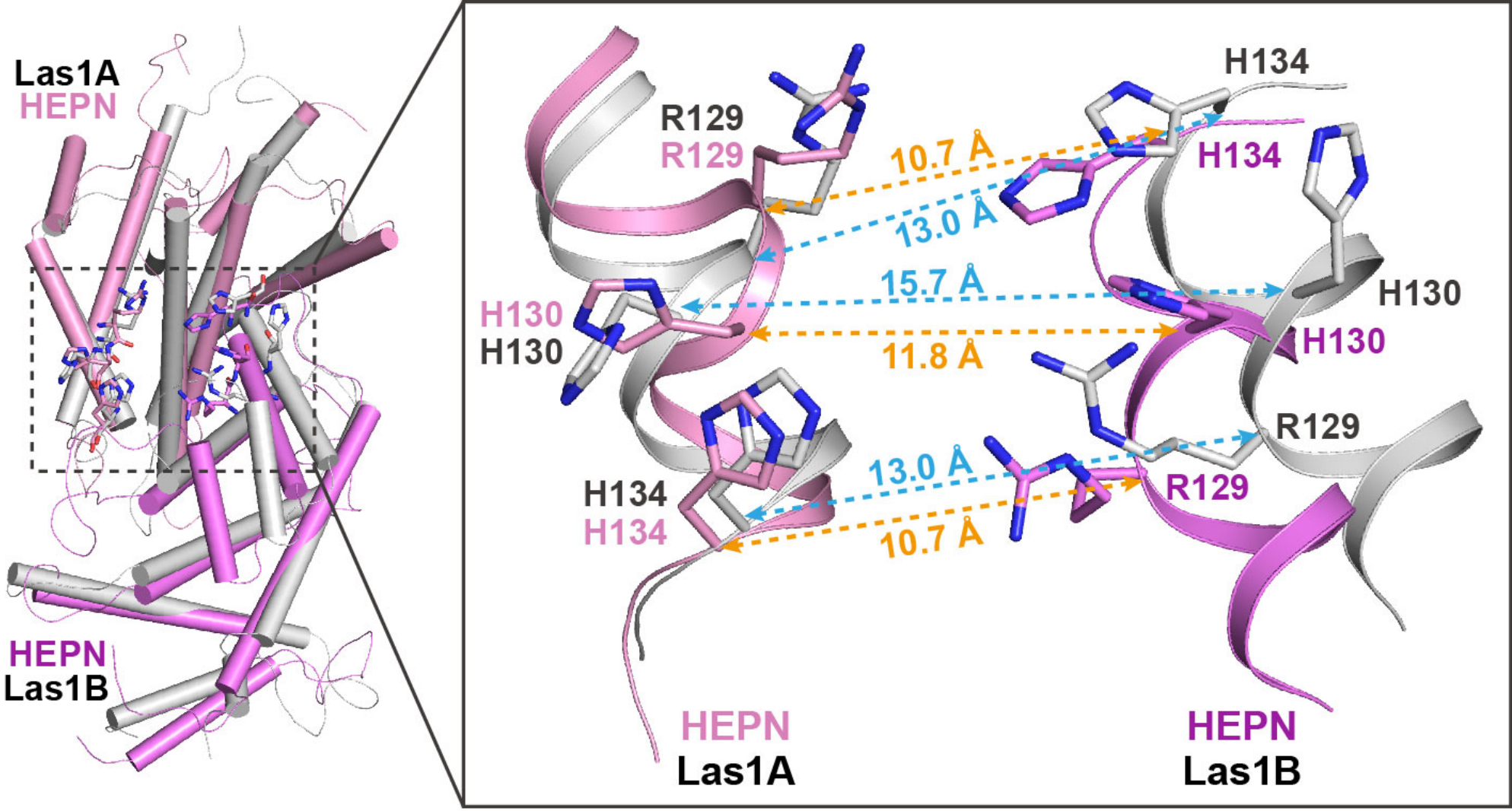

Figure 7—figure supplement 2

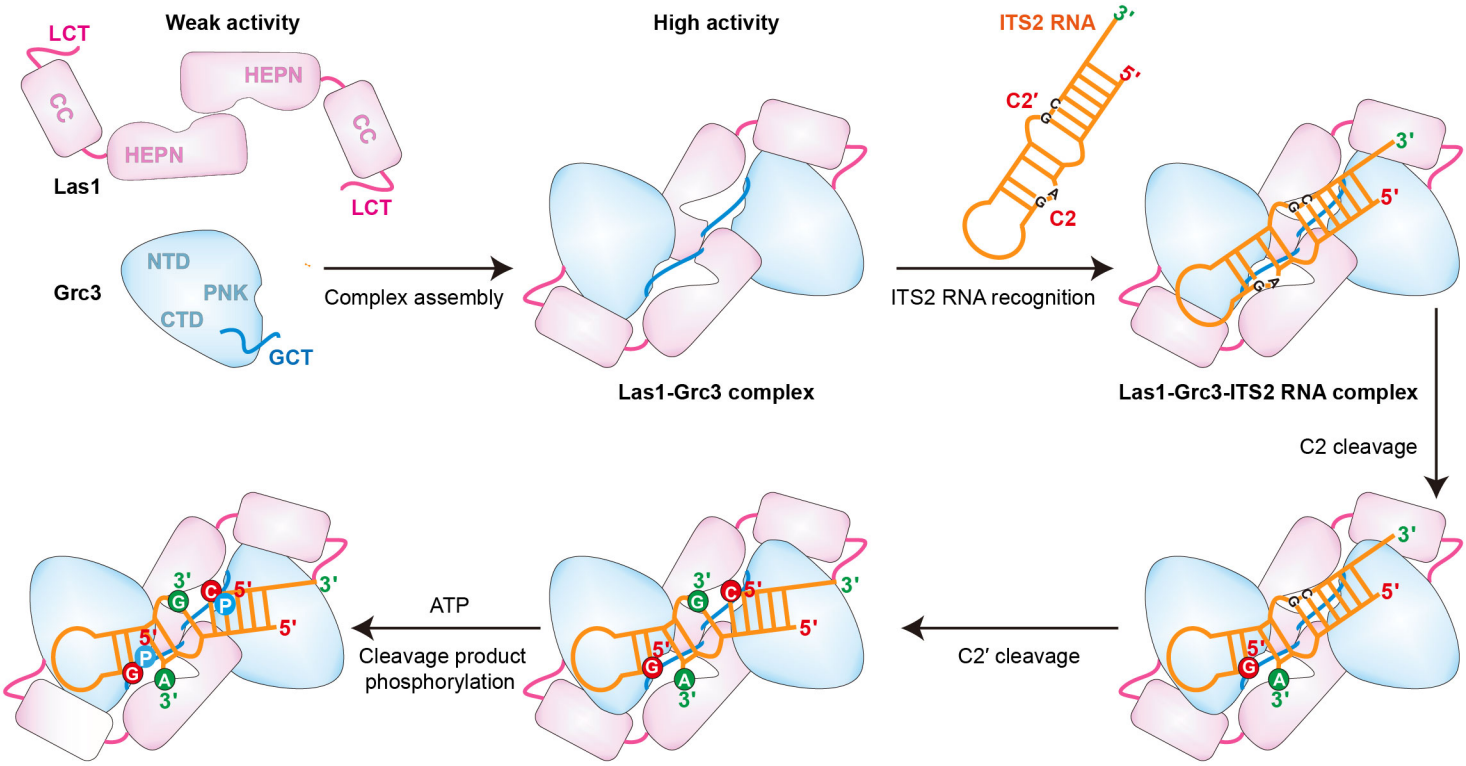
Weak activity
High activity
LCT
HEPN
CC
HEPN
CC
LCT
Las1
Grc3
NTD
PNK
CTD
GCT
Complex assembly
Las1-Grc3 complex
ITS2 RNA
3'
5'
C2'
C2
ITS2 RNA recognition
Las1-Grc3-ITS2 RNA complex
C2 cleavage
C2' cleavage
ATP
Cleavage product phosphorylation
G
C
A
P

Figure 8

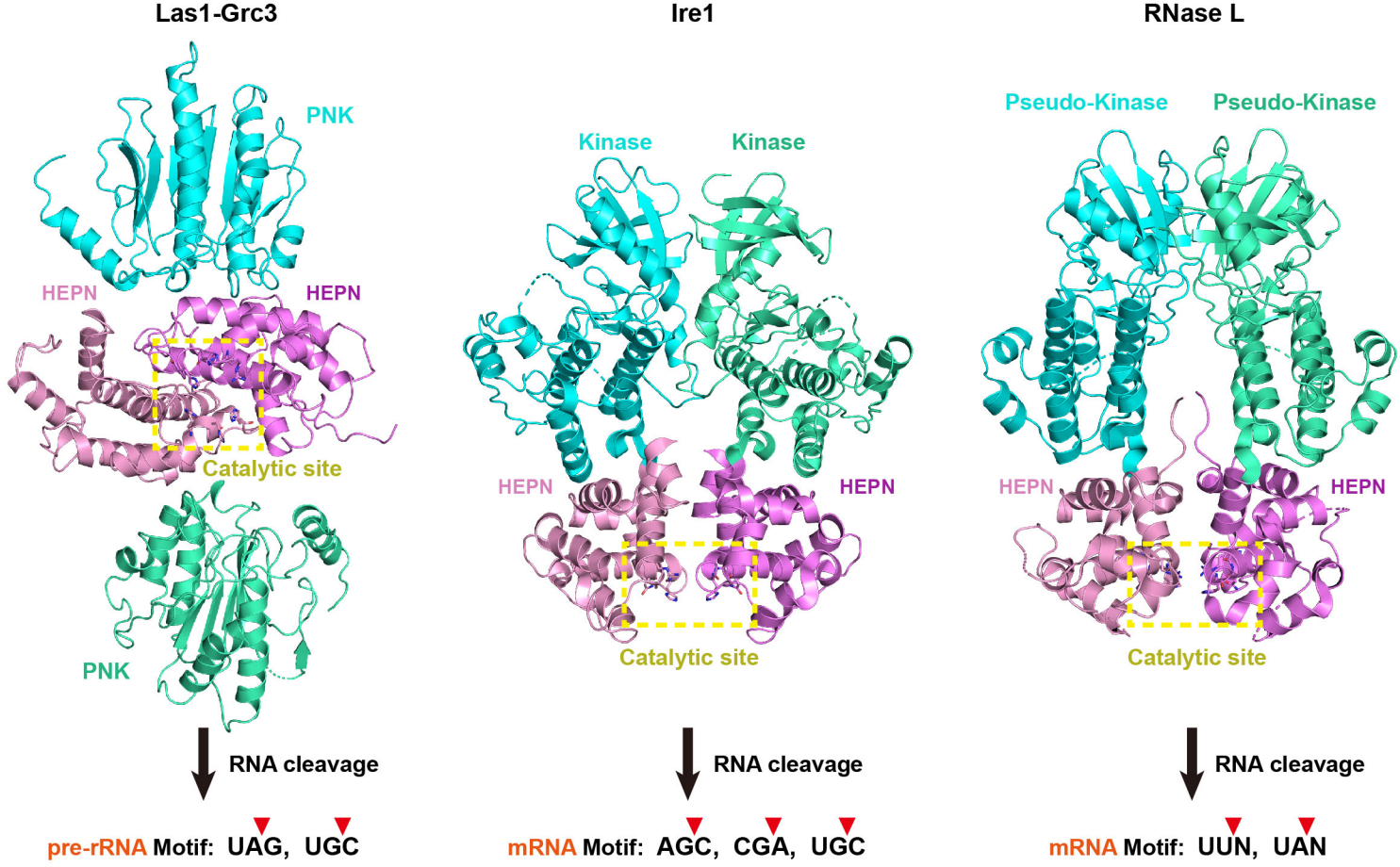

Figure 8—figure supplement 1